

# Drivers of Subsurface Temperature Variability in the Northern California Current

 S. Ray<sup>1</sup> , S. A. Siedlecki<sup>1</sup> , M. A. Alexander<sup>2</sup> , N. A. Bond<sup>3,4</sup> , and A. J. Hermann<sup>3,4</sup> 

<sup>1</sup>Department of Marine Sciences, University of Connecticut, Groton, CT, USA, <sup>2</sup>Physical Sciences Laboratory, NOAA, Boulder, CO, USA, <sup>3</sup>University of Washington, Joint Institute for the Study of the Atmosphere and Ocean, Seattle, WA, USA, <sup>4</sup>Pacific Marine Environmental Lab (PMEL), NOAA, Seattle, WA, USA

**Special Section:**

Advancing Prediction of Coastal Marine Ecosystems

**Key Points:**

- Oceanic teleconnections originating in the North Pacific dominate the northern CCS subsurface temperature variance in a linear model
- Oceanic teleconnections via west-central and eastern Pacific spine variations influence the subsurface temperature variance
- Coastally trapped waves originating from the equator during ENSO years influence the N-CCS subsurface temperature variability

**Supporting Information:**

- Supporting Information S1

**Correspondence to:**

 S. Ray,  
sulagna.ray@gmail.com

**Citation:**

Ray, S., Siedlecki, S. A., Alexander, M. A., Bond, N. A., & Hermann, A. J. (2020). Drivers of subsurface temperature variability in the Northern California Current. *Journal of Geophysical Research: Oceans*, 125, e2020JC016227. <https://doi.org/10.1029/2020JC016227>

Received 9 MAR 2020

Accepted 26 JUL 2020

Accepted article online 4 AUG 2020

**Abstract** JISAO's Seasonal Coastal Ocean Prediction of the Ecosystem (J-SCOPE) was developed to carry out experimental seasonal forecasts of ocean conditions in the Northern California Coastal System (N-CCS). This system relies on NOAA's Coupled Forecast System (CFS) global climate model to provide initial and boundary conditions for dynamical downscaling with a high-resolution numerical ocean model. Experiments with J-SCOPE show that the bottom temperature on the shelf is more predictable than the sea surface temperature (SST) on seasonal time scales. While seasonal forecasts have been shown to have positive skill in terms of SST for the CCS due to El Niño-Southern Oscillation (ENSO), the mechanism(s) responsible for subsurface predictability in the N-CCS have yet to be determined. This study quantifies the relative importance of North Pacific and Tropical Pacific properties in determining the variations in temperatures at depth (TDs) on the N-CCS shelf. A multivariable linear regression (MLR) model with selected predictors explains almost 83% of the N-CCS TD variability with oceanic teleconnections from the North Pacific dominating the variance. The N-CCS TD is related to (i) coastally trapped waves (CTWs) related to ENSO, originating in Tropical Pacific, (ii) west-central Pacific spine anomalies, (iii) seasonal Pacific Decadal Oscillation (PDO) variation, and a more local influence from (iv) anomalies south of N-CCS, originating in North Pacific. ENSO and CTW can each impact the depth of the California Undercurrent (CUC) core with the latter most prominently following ENSO events. The results on potential sources of predictability are relevant to the continued development of current seasonal forecasting efforts off the U.S. West coast.

**Plain Language Summary** The Washington/Oregon shelf is a productive habitat with important commercial fisheries. One of the most valuable species is Dungeness crab, which resides on the subsurface shelf and is sensitive to near-bottom ocean properties such as temperatures and oxygen concentrations. The predictability of these properties on seasonal time scales is being investigated using JISAO's Seasonal Coastal Ocean Prediction of the Ecosystem (J-SCOPE). Previous studies have explored the driving mechanisms of surface temperature predictability, with a focus on linkages to ENSO; this study investigates their counterparts for subsurface temperatures. We find that remote forcings primarily from the North Pacific have strong influences on the subsurface temperatures. A relatively simple statistical model explains 83% of the subsurface temperature variability. The results on potential sources of predictability are relevant to the continued development of current seasonal forecasting efforts off the U.S. West Coast.

## 1. Introduction

Living marine resources (LMRs) respond to climate variability, and the managers and stakeholders of these LMRs are beginning to seek guidance from developing prediction systems to enrich their decision-making capabilities (Tommasi et al., 2017). Some commercially important species, like the Dungeness crab, reside predominantly near the bottom and are largely influenced by deep shelf conditions. Forecasting subsurface coastal conditions in support of LMRs relies on understanding the physical mechanisms driving the forecast skill—the atmosphere and ocean dynamics, as simulated in models (Jacox et al., 2020). Dynamic and statistical predictions of ocean conditions along the U.S. West Coast have been studied to understand and improve forecast skill (Chenillat et al., 2012; Crawford et al., 2018; Hervieux et al., 2017; Jacox et al., 2017; Kirtman et al., 2014; McClatchie et al., 2009; Siedlecki et al., 2016; Stock et al., 2015), but work done to understand the sources of their predictive skill has focused on surface conditions. Recent work has shown that the predictability of subsurface temperature differs from sea surface temperature (SST) in the Northern California

Current System (N-CCS) using JISAO's Seasonal Coastal Ocean Prediction of the Ecosystem (J-SCOPE) (Siedlecki et al., 2016). Although predictability due to factors other than El Niño-Southern Oscillation (ENSO) does exist in the North Pacific (Capotondi et al., 2019), seasonal forecasts of CCS SST have been shown to have positive skill due to ENSO (Jacox et al., 2017; Stock et al., 2015).

Mechanisms that control the CCS variability, particularly its strong seasonal upwelling (Bograd et al., 2019; Hickey et al., 2016; McCabe et al., 2015), have been widely studied, but mechanisms that drive seasonal predictability have only recently been investigated. Subsurface water properties in the N-CCS are known to vary differently than surface conditions, as seen through moored observations (Hickey et al., 2016). Mechanisms are typically categorized into local versus remotely driven processes (Jacox, Bograd, et al., 2015) but can be both, as well. For example, the alongshore winds related to coastal upwelling are a local effect but are also strongly associated with basin-scale modes such as the Pacific Decadal Oscillation (PDO) and North Pacific Gyre Oscillation (NPGO) (Chhak & Di Lorenzo, 2007; Chhak et al., 2009; Combes et al., 2013; Di Lorenzo et al., 2008).

It has long been realized that ENSO strongly influences CCS ocean properties (Bograd et al., 2019; Hermann et al., 2009; Huyer & Smith, 1985; Jacox, Fiechter, et al., 2015; Lynn et al., 1995; Schwing et al., 2002) and transmits signals to the N-CCS in more than one way. On seasonal time scales, its effect is communicated via (i) atmospheric pathways (i.e., atmospheric teleconnections to the North Pacific climate influencing surface heat fluxes, Ekman transport, and wind-driven upwelling anomalies) (Alexander & Scott, 2008; Alexander et al., 2002; Jacox et al., 2017) and (ii) oceanic teleconnections (i.e., oscillations in the thermocline driven by coastally trapped waves [CTWs]) (Enfield et al., 1987; Lyman & Johnson, 2008; Melsom et al., 2003; Meyers et al., 1998). The atmospheric teleconnections (i) have been largely the focus of recent work on drivers of CCS SST predictive skill (Jacox, Fiechter, et al., 2015; Jacox et al., 2017, 2018), but the oceanic teleconnections and their role as source of predictive skill have not yet been explored.

The oceanic teleconnections involve principally ENSO-driven variability transmitted to the CCS via CTW. The generation of equatorial Kelvin waves in the western equatorial Pacific prior to an El Niño/La Niña event excites downwelling/upwelling waves that then suppresses/shoals the equatorial thermocline as it propagates eastward and northward along the North American coast (Engida et al., 2016; Flores-Morales et al., 2012; Frischknecht et al., 2015; Hickey et al., 2003, 2006; Hermann et al., 2009; Thomson & Krassovski, 2010). A propagating Kelvin wave can feature a downwelling Kelvin wave that depresses the isopycnals, whereas an upwelling wave shoals the isopycnals, bringing cooler subsurface waters closer to the surface. Remotely driven CTWs that narrow going poleward and diminish moving away from the equator can be tracked all the way to the Gulf of Alaska and explain a large variance of the sea surface height (SSH) (Hermann et al., 2009) and surface physical properties in the central and northern CCS (Frischknecht et al., 2015). The Kelvin waves propagate quickly but are produced in multiple bursts over several months (Meyers et al., 1998), resulting in isopycnal displacements that can persist for months (Jacox, Fiechter, et al., 2015).

On longer time scales, source waters from the subarctic, subtropical, and the eastern equatorial Pacific can be advected in and influence the long-term water properties upwelled onto the shelf of CCS via regionally important currents (Bograd et al., 2015, 2019; Freeland et al., 2003; Huyer, 2003; Kosro, 2003; Meinvielle & Johnson, 2013; Pozo Buil & Di Lorenzo, 2017; Thomson & Krassovski, 2010). Warm equatorial source waters flow poleward within the California Undercurrent (CUC), transporting heat and chemical tracers, and serve as a source of upwelled nutrients into the CCS (Connolly et al., 2014; Garfield et al., 2001; MacFadyen et al., 2008). Although the strength of the CUC is constantly modified as it moves poleward (Pelland et al., 2013), the CUC retains the potential to influence the seasonal water properties off the N-CCS (Hickey et al., 2016), in particular via its depth modulation, which affects the upwelled water properties (Combes et al., 2013; Hickey et al., 2016; Stone et al., 2018). On decadal time scales, eastward advection from Kuroshio-Oyashio regions (Kouketsu et al., 2017; Sasaki et al., 2010; Taguchi & Schneider, 2014) advects spiciness anomalies (density-compensated water mass properties) towards the U.S. West Coast. Eastward propagation of anomalies has been identified as a potential source of predictability for CCS productivity (Pozo Buil & Di Lorenzo, 2017; Rykaczewski & Dunne, 2010). All of these oceanic teleconnections influence the variability of subsurface temperatures in the N-CCS; however, the relative importance of each of these mechanisms has yet to be determined.

This study quantifies the relative importance of North Pacific and Tropical Pacific factors in determining the variability of subsurface temperatures on the shelf of the N-CCS. For that purpose, we use data from NOAA's Climate Forecast System Reanalysis (CFSR) (Saha et al., 2010) to specify oceanic variables and a multivariable linear regression (MLR) model to investigate the linkages between oceanic variables (and ocean climate indices) and subsurface temperatures in the N-CCS. J-SCOPE relies on a related product, namely, predictions from NOAA's Coupled Forecast System (CFS) global climate model to provide initial and boundary conditions for dynamical downscaling with a high-resolution numerical ocean model (Kaplan et al., 2016; Siedlecki et al., 2016). Our analysis therefore indicates the large-scale oceanic properties representing sources of predictability for the J-SCOPE domain. The paper is organized as follows: section 2 introduces the CFS data set and describes the various methods used in analyzing the data set, including how subsurface temperature relevant to the N-CCS shelf is defined in the data set, the use of Hovmöller diagrams to determine propagation, and a description of the MLR method. Section 3 presents results organized by time scale in terms of their influences on the N-CCS subsurface temperatures. Finally, section 4 discusses the results of the paper in the context of prior studies, followed by concluding remarks in section 5.

## 2. Data and Methods

### 2.1. Climate Forecast System Reanalysis

NOAA's Climate Forecast System Reanalysis (CFSR) (Saha et al., 2010) and Operational Analysis assimilate in situ and satellite observations of the atmosphere and ocean into a global, coupled model using the 3DVAR technique, and the monthly averaged product is used here over the period of 1979–2017 for analysis. The CFS forecast fields are used as boundary conditions to the J-SCOPE forecast system (Siedlecki et al., 2016); hence, it is relevant to investigate the reanalysis for mechanisms linking large-scale circulation via the boundaries of the J-SCOPE domain.

CFSR's resolution (25–50 km) is not sufficient to resolve the shelf topography off the Washington/Oregon coast. However, using Regional Ocean Modeling (ROMS, Rutgers version 3) (Giddings et al., 2014) with a higher horizontal resolution (1.5 km) and 40 vertical levels, the J-SCOPE forecast system resolves the shelf-slope bathymetry in much greater detail (supporting information, Figure S1). We refer to the domain covered by J-SCOPE (43°N to 50°N; 128°W to 122°W) as the N-CCS for the rest of the paper. Both CFSR and J-SCOPE reasonably capture the seasonal displacements of the isopycnals—shoaling during upwelling season of August and deepening during downwelling season of December (Figure S1). The  $26.4\sigma$  isopycnal is within the pycnocline depth in the North Pacific and a reasonable depth to serve as an index of the thermocline variability. Referring to the temperature along the time-varying  $26.4\sigma$ , averaged over the N-CCS domain as the temperature at depth (TD), we discuss mechanisms controlling its variability in the rest of the paper. Essentially, TD serves as our index of N-CCS bottom temperature.

### 2.2. Simple Ocean Data Assimilation 3.4.2

The Simple Ocean Data Assimilation (SODA) ocean/sea ice reanalysis (version 3, SODA3, Carton et al., 2018) is used as an additional data set for MLR evaluation. SODA3 consists of an ensemble reanalysis. The reanalysis uses the ocean model GFDL/MOM5 with eddy-permitting resolution (10–28 km). In this study, we use the latest version of the ensemble reanalysis, SODA 3.4.2, which is forced by ERA-I atmospheric reanalysis. The monthly averaged product remapped on the regular  $0.5^\circ \times 0.5^\circ$  Mercator horizontal grid is used over the period 1980–2016.

### 2.3. Spiciness

In contrast to potential temperature or salinity anomalies, which have a dynamical feedback on the circulation due to their association with density anomalies, spiciness retains the conservative properties of salinity and temperature while acting like a passive tracer along density surfaces. Consequently, spiciness was chosen here to represent water mass properties along isopycnals. The concept of spice relies on the fact that along fixed isopycnals, the effects on density due to changes in temperature are compensated by changes in salinity (McDougall & Krzysik, 2015). Hence, warm, salty (spicy) equatorial source water from south could have similar density as the cold, fresher (minty) Arctic water from the north of N-CCS, in spite of different characteristics. Variations in sea water properties along fixed isopycnals can be traced using a linear combination of temperature and salinity, which is orthogonal to the isopycnals in temperature-salinity

space. Spiciness is that measure, with units of kilogram per cubic meter, and is thus appropriate to examine changes along an isopycnal (Timmermans & Jayne, 2016). It is calculated here from Gibbs Seawater Oceanographic Toolbox using the International Thermodynamics Equation of Seawater (TEOS-10; IOC et al., 2010; McDougall & Barker, 2011; Timmermans & Jayne, 2016).

#### 2.4. Analysis Method

Anomalies of spice and temperature are analyzed after removing the seasonal cycle (12-month climatology) for the period 1979–2017 in CFSR data and for the available period of 1980–2016 in SODA 3.4.2 data. Monthly anomalies are analyzed for all years (1979–2017), neutral years (12 years), and ENSO years (18 years), including both warm and cold events, in addition to seasonal averages, such as March–April–May (MAM), May–June–July (MJJ), and October–November–December (OND). ENSO years are selected based on the NOAA-defined Oceanic Niño Index (ONI, 3-month averaged SST anomaly in 170°W to 120°W, 5°S to 5°N; ONI greater (less) than 0.5°C (−0.5°C) is considered an El Niño (La Niña) event). Given the small sample size, 10 El Niño and 8 La Niña events, we combine them together as ENSO (10 + 8 = 18) events and examine the (linear) effects from both El Niño and La Niña conditions. To identify propagating signals across the North Pacific and along the U.S. West Coast, we use Hovmöller diagrams of monthly anomalies along fixed latitudes as well as along diagonal sections. The diagonal sections extend across different latitudes between the Kuroshio-Oyashio region in the West Pacific and the Pacific Northwest in N-CCS along 36°N, 160°E to 51°N, 128°W. A second Hovmöller diagram is done along a transect that hugs the coastline, drawn between the equatorial Pacific and the Gulf of Alaska along the U.S. West Coast, between 0°N, 70°W and 60°N, 150°W. The first Hovmöller diagram is used to demonstrate the propagation of monthly spice anomalies along the 26.4 $\sigma$  surface and the second to show propagation of the CTWs as represented by the monthly 26.4 $\sigma$  depth anomalies.

In this study, we focus on mechanisms that potentially provide predictability to the N-CCS subsurface temperature, as identified using spatial correlation analysis at various temporal lags. Significance of correlations is estimated using a one-sided student *t* test, where the serial autocorrelation has been included in the computation of the effective degrees of freedom following Bretherton et al. (1999). This method has been earlier used in Ray et al. (2015) to test significance of correlations in subsurface temperatures between multiple re-analyses. The effects of large-scale atmospheric influence associated with the PDO are also included. Disentangling the seasonal effects of ENSO and PDO due to their overlapping relationships with the Aleutian Low fluctuations can be difficult. However, some of the processes contributing to the PDO can differ from those associated with ENSO teleconnections (Newman et al., 2016; Wills et al., 2018) and could independently influence the N-CCS ocean conditions via atmospheric pathways. As such, we treat them separately in the predictor selection.

#### 2.5. Persistence

Persistence of monthly N-CCS TD variability is calculated using lagged autocorrelation for all months (Deser et al., 2003) over the period 1979–2017. A monotonic decrease in the autocorrelation of TD gradually flattens at around 25 months (Figure S2), indicating the time scale of persistence. Hence, a lag of 25 months in TD is used to represent the persistence (*persis*), an input for the MLR model, as discussed in the following sections.

#### 2.6. Multivariable Linear Regression

To determine the relative importance of the potential predictors to N-CCS TD variability, an MLR model with predictors based on spatial correlation analysis at various lags is used to reconstruct the monthly (and annually smoothed) N-CCS TD for 1979–2017. While the relationships between TD and its predictors are not necessarily linear, we also do not expect them to be highly nonlinear, and hence, an MLR seems to be a reasonable method for exploring the linkages (He & Guan, 2013; Jacox et al., 2018). The model does not include predictors that explain local mechanisms (except for local persistence of TD) within the N-CCS, but is used to diagnose the relative importance of remote regions and physical mechanisms as represented by the spatial correlation analysis to the variability of the N-CCS TD. Analysis based on lagged correlations (exceeding 90% significance, where the serial autocorrelation has been taken into account for the computation of the degrees of freedom following Bretherton et al., 1999) of TD to the spiciness patterns of North Pacific and Tropical Pacific is used to identify potential predictor variables. However, if regions were



**Table 1**  
*Table of Predictors as Input in MLR*

Predictor name	Definition—spatial averages of anomalies	Time lag
WP6	Spice in 160°E to 175°E, 37°N to 43°N	6 years
WP5	Spice in 160°E to 175°E, 37°N to 43°N	5 years
SCP5	Spice in 178°E to 170°W, 37°N to 43°N	5 years
SCP4	Spice in 178°E to 170°W, 37°N to 43°N	4 years
SB2	Spice in 136°W to 125°W, 35°N to 41°N	2 years
SB1	Spice in 136°W to 125°W, 35°N to 41°N	6 months
PDO7	EOF1 of SST in 120°E to 100°W, 20°N to 60°N	7 years
PDO4	EOF1 of SST in 120°E to 100°W, 20°N to 60°N	4 months
Nino3	SST in 170°W to 120°W, 5°S to 5°N	4 months
Persis	N-CCS temperature at depth (TD)	25 months

identified and a physical mechanism could not be tied to the region or time scale, the predictor was discarded prior to input in the MLR as a potential statistical artifact.

Multiple predictor variables increase the precision of estimated coefficients, as well as the skill in representing the predicted value. The automated stepwise linear regression function in MATLAB (R2019a; stepwiselm) is used to evaluate the combination of predictors by adding/removing them until the best linear fit with the lowest Akaike's Information Criteria corrected (AICc; Burnham & Anderson, 2002; Yamashita et al., 2007) score is obtained (Norton et al., 2020). The benefit of using AICc scores for model selection is that AICc imposes a penalty for variable inclusion to prevent overfitting and subsequent declines in model prediction performance and, as such, attempts to balance the inclusion of additional predictor variables that improve model fit but result in increased model complexity (Wilks, 1995). All predictors ( $p =$

10) identified in the spatial correlation analysis are brought into this analysis; the full list is provided in Table 1 (section 3.4.1). This is followed by deselecting predictors using variance inflation factor (VIF) to check for collinearity among them, thus producing a set of independent predictor variables. This process is repeated until the AICc is minimized. Similar methods (AIC, VIF) were earlier used to determine two predictors for aragonite saturation state from multiple variables (Juraneck et al., 2009). In summary, we arrive at a parsimonious model selection following the following steps: (i) reduction in AICc score and (ii) deselecting each predictor for collinearity with highest VIF score. Repeating the steps until the AICc is minimized, we determine the normalized coefficients of the selected predictors in the final model selection to compare the relative contribution of each predictor. The coefficients are normalized by multiplying them to the ratio of the standard deviation in the selected predictor and the predictand (N-CCS TD). This process is done at the monthly time scales ( $N = 468$ ) and the corresponding annually smoothed time series ( $N = 456$ ) that decreases the number of predictand by 12. In the end, we produce an MLR for the monthly time series and its annually smoothed time series of the N-CCS TD variability composed of independent predictors with normalized coefficients which allows us to determine the relative importance of each predictor for the region.

### 2.7. MLR Evaluation

The MLR in section 2.6 is evaluated with the SODA 3.4.2 data set, which is not used in the parsimonious model selection/calibration, in order to confirm that the mechanisms, regions, and time lags identified in CFSR are robust influences on N-CCS TD variability. The evaluation is done in two ways: (i) using the coefficients of the selected predictors from CFSR (section 3.4.2), with predictors identified in CFSR but sampled from the regions of the SODA 3.4.2 data set, to assess the MLR performance and (ii) using only the selected predictors from CFSR (section 3.4.1), but sampling from regions of the SODA 3.4.2 data set and refitting the coefficients to be SODA 3.4.2 specific, as a means of assessing the relative importance of the predictors to the N-CCS TD variability in the reanalysis. This second method is employed to account for any model differences between the reanalyses that may influence the results of (i). The monthly anomaly fields of temperature and spiciness for the period 1980–2016 are derived by removing the climatology of the same period. The predictor variables are defined from these anomaly fields to verify the MLR in section 3.4.2 for (i). A linear regression of the N-CCS TD from these predictors is calculated to evaluate (ii). Additionally, evaluation of the MLR over time is also performed by refitting the MLR with the selected predictors (section 3.4.1) from 1979 to 2010 and then comparing the resulting MLR to the CFSR N-CCS TD variance over the period 2011–2017. The  $R^2$  value is used in all the cases to evaluate the predictor fitted on the MLR to N-CCS TD from SODA 3.4.2 and CFSR.

## 3. Results

To determine the role of existing drivers of variability in the Pacific in driving the N-CCS TD variability, spatial correlations with physically relevant time lags were performed to identify potential predictors. Their relative importance was determined through construction of an MLR of the N-CCS TD using monthly

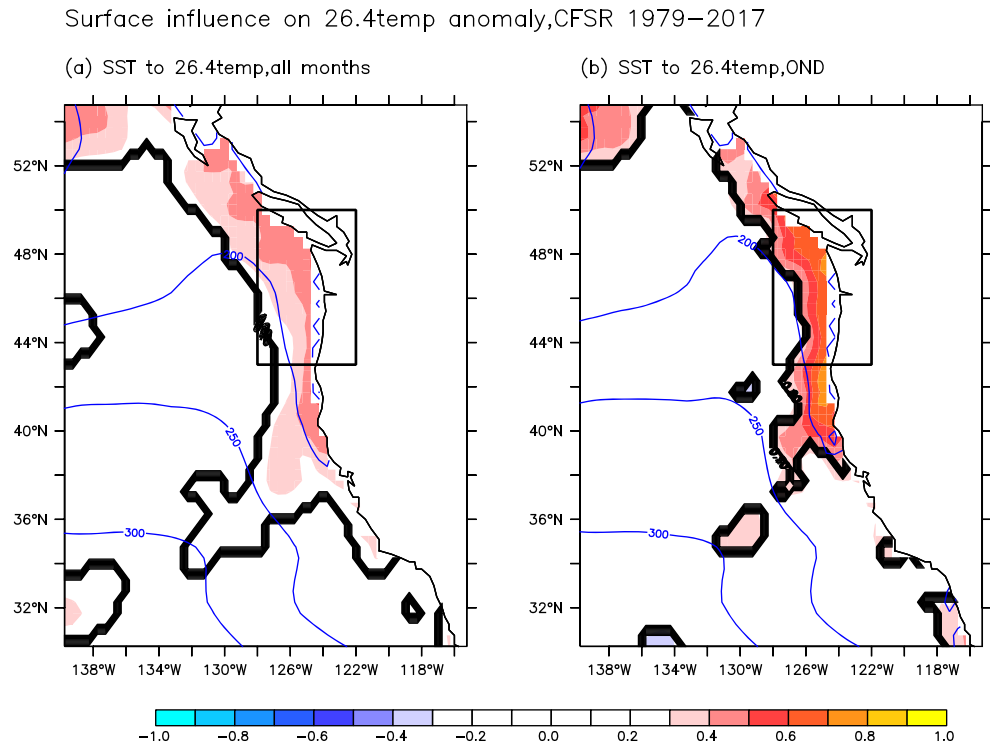


**Figure 1.** Correlation of surface temperature with 26.4 $\sigma$  temperature. Shading indicates the intensity of the correlation between (a) monthly SST anomalies and monthly 26.4 $\sigma$  temperature anomalies and (b) 3-month averaged (OND) SST anomalies and 3-month averaged (OND) 26.4 $\sigma$  temperature anomalies. Ninety percent significant correlation is contoured in bold black, and thin blue contours denote the mean depth of 26.4 $\sigma$  at an increment of 50 m.

fields. Because CFSR was relied on for these analyses, we first review the performance of CFSR in the North Pacific and CCS region (section 3.1). Next, we identify and validate the use of the 26.4 $\sigma$  isopycnal surface from CFSR for investigating oceanic teleconnections with the N-CCS region (section 3.2). The main section of the results details the identification of potential predictors from the spatial correlation analysis. Finally, the identification of the final predictors for the development of the MLR at both the annual and monthly time scales is presented (section 3.4). The MLR is also evaluated with respect to the independent data set from SODA 3.4.2 (section 3.5).

### 3.1. Performance of CFSR in the CCS

The performance of the CFSR in the North Pacific and Tropical Pacific including simulating ENSO variability has already been assessed in prior studies (Saha et al., 2010; Xue et al., 2011). We briefly review and provide additional analysis of CFSR's performance in simulating the seasonality in CUC in N-CCS domain in Appendix A1.

### 3.2. Representation of 26.4 $\sigma$ as the Surface for Investigating Oceanic Teleconnections

The 26.4 $\sigma$  isopycnal is within the depth of the pycnocline; however, mixing processes and vertical velocities associated with winter downwelling along the Pacific Northwest margin could allow communication between the surface and the 26.4 $\sigma$  isopycnal. Indeed, most of the surface influence on 26.4 $\sigma$  temperature occurs during the fall/winter months (Figure 1). Following the reemergence mechanism (Alexander & Deser, 1995; Alexander et al., 1999; Byju et al., 2018), winter prior SST anomalies are significantly correlated to the following summer 26.4 $\sigma$  temperature anomaly. However, the negative correlation of winter SST anomalies to the concurrent downward surface heat fluxes (not shown) suggests that the former is not entirely surface driven. This indicates that near the coast, subsurface processes that occur below the mixed layer influence SST and surface fluxes during fall/winter months in addition to the atmosphere. We leave further identification of this mechanism for future studies and conclude that the 26.4 $\sigma$  layer is deep

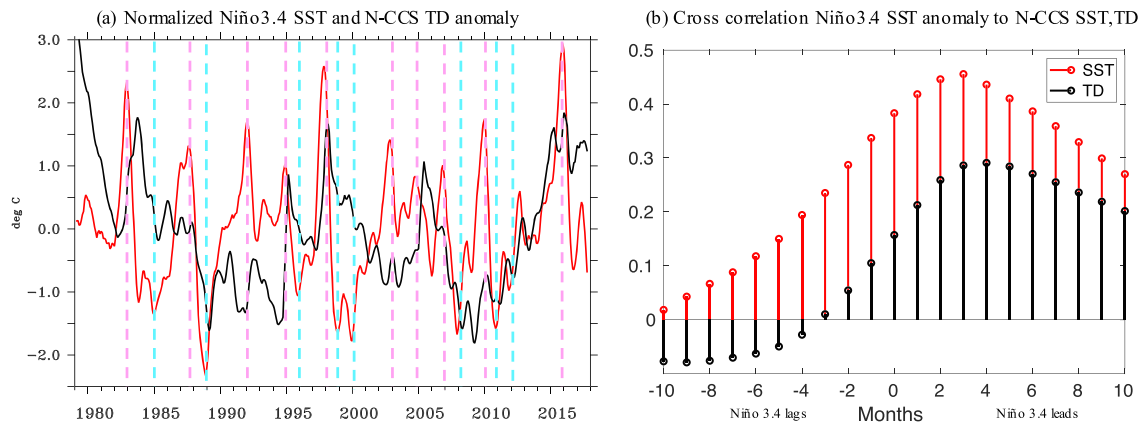


**Figure 2.** N-CCS follows Niño 3.4 SST. (a) Time series of normalized Niño 3.4 SST monthly anomaly (red) and N-CCS monthly temperature anomaly at depth (TD, averaged temperature along  $26.4\sigma$ , black) in CFSR, 1979–2017, with magenta and blue vertical lines marking the El Niño and La Niña years. Time series are smoothed over 5 months with a boxcar filter. (b) Lagged cross correlation of monthly Niño 3.4 SST anomaly to N-CCS averaged monthly SST (red) and N-CCS TD (black) anomaly for all months. No smoothing applied in (b).

enough (150–200 m) to represent an oceanic pathway of influence. It retains the seasonal coastal upwelling variability (not shown) and is a reasonable depth for the CUC core (MacFadyen et al., 2008, Stone et al., 2018; further discussed in Appendix A1).

### 3.3. Spatial Correlation Analysis: Identification of Potential Predictor Variables

Spatial correlations from analyzing monthly CFSR reanalysis are used to identify several regions and time lagged correlations of interest as potential predictors for the linear regression model of N-CCS TD variability. Although each of the variables of interest is linked to an established oceanic teleconnection or region of known influence on N-CCS TD, not all are statistically selected as predictors in the stepwise linear model. In the following sections, we highlight the spatial correlation analysis used to identify the potential predictors, beginning with the seasonal time lag and examining longer time lags.

#### 3.3.1. ENSO-Associated CTWs

The interannual variability in TD is associated with ENSO, as represented by its close association to Niño 3.4 SST variations. The peak anomalies of TD follow the peaks of ENSO events with a delay of 4 months later (Figure 2a). The N-CCS SST experiences a peak correlation at a lag of 3 months, but the N-CCS TD experiences a lag of 4 months after the Niño 3.4 SST anomaly (Figure 2b). This time scale is not consistent with advection from the equatorial Pacific, which would take years. One mechanism fast enough to transport this signal subsurface is CTW, which has been previously identified as being shed more often during ENSO events. Local atmospheric variability associated with ENSO could also be responsible.

CTW generated south of N-CCS domain propagates northward, perturbing the isopycnals (Figures 3 and 4). The variability in N-CCS  $26.4\sigma$  is closely associated with the  $26.4\sigma$  variations south of N-CCS extending all along the coast to the central equatorial Pacific as shown by the correlations (Figure 3a). Significant correlations strengthen and narrow along the coastline from the equator following ENSO years (Figure 3c), but are significant only along the U.S. West Coast and do not extend from the equator for neutral years (Figure 3b). This suggests that remote generation of seasonal CTW from the equatorial Pacific is more influential during ENSO years than during neutral years on TD variability. High correlations of N-CCS  $26.4\sigma$  variations to the alongshore wind stress south of the domain following neutral years only are suggestive of local generation of CTWs during that time interval (not shown).

Following ENSO years only, significant correlations exist between the N-CCS depth averaged temperature and the entire U.S. West Coast depth of the  $26.4\sigma$ . N-CCS MAM averaged temperatures between 150 to 250 m are significantly correlated to the depth of  $26.4\sigma$  during the OND averaged prior (4 months) along the southern CCS and extending to the equatorial Pacific during ENSO years (Figure 3f). Such correlations are absent during neutral years (Figure 3e). These correlations are suggestive of separate mechanisms of CTW influence during ENSO and neutral years. The influence of ENSO via an oceanic teleconnection

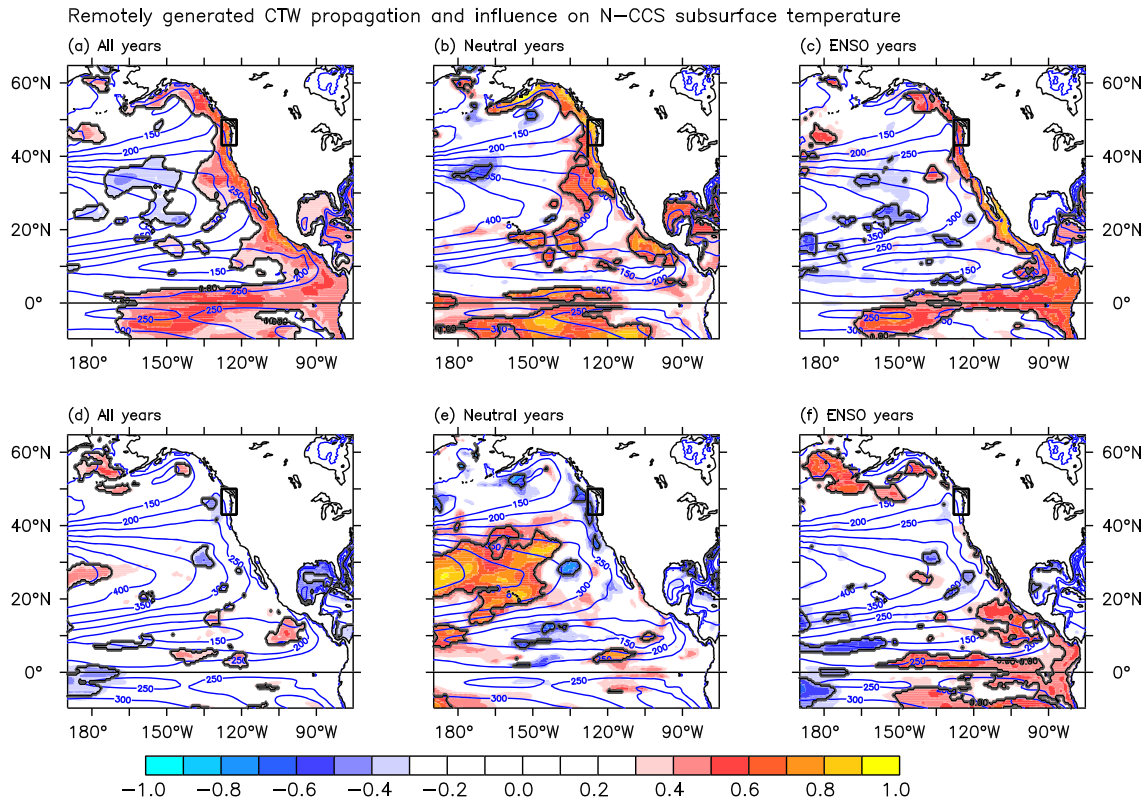


**Figure 3.** Remotely driven CTW influence on N-CCS TD. Spatial correlations of (a–c) N-CCS depth of MAM  $26.4\sigma$  to prior OND depth of  $26.4\sigma$ , and (d–f) N-CCS MAM temperature at 150–250 m (box) to OND (4 months prior) depth of  $26.4\sigma$  for (a, d) all years, (b, e) neutral years, and (c, f) ENSO years (10 El Niño + 8 La Niña events). Shading indicates the magnitude of the correlations, with regions of 90% significant correlations enclosed by bold black contours. Blue contours denote the mean depth of  $26.4\sigma$  at an increment of 50 m. Significant continuous correlations along the coast from equator to N-CCS (a, c) suggest that propagating equatorial Kelvin waves (shown in Figure 4) reach the N-CCS domain in the following spring and that these waves significantly influence the N-CCS subsurface following ENSO years (f).

consisting of CTW is apparent from these correlations, but the time scale is a bit longer than expected for that mechanism as identified in prior work (Jacox et al., 2020).

ENSO events are generally accompanied by multiple rather than single Kelvin waves (Meyers et al., 1998). The continuous shedding of multiple waves moving up the coast could cause longer periods of deepening/warming (Frischknecht et al., 2015). A composite Hovmöller diagram of all the ENSO events for the  $26.4\sigma$  depth anomalies reveals that CFSR simulates the propagation of the waves from equatorial Pacific (Figure 4). The time scale for this oceanic teleconnection to influence the N-CCS can be estimated from known CTW propagation speeds. From Niño 3.4 region ( $170^{\circ}\text{W}$  to  $120^{\circ}\text{W}$ ;  $5^{\circ}\text{S}$  to  $5^{\circ}\text{N}$ ), it takes around 1.5 month for equatorial Kelvin waves to reach the South American coast at a speed of 2.8 m/s and another 1.5 month to reach the N-CCS at a speed of 2 m/s. Thus, Niño 3.4 SST variability lagged by 4 months contributes to the N-CCS TD variability and is chosen here to represent an ENSO teleconnection. We henceforth refer to it as *Nino3* and include it as a potential predictor for the linear regression model.

### 3.3.2. CUC Depth Changes

The seasonal and interannual variations in the depth of CUC have been argued to influence the shelf properties in the N-CCS (Stone et al., 2018) through the source depth of upwelled water. Consistent with this idea, N-CCS averaged subsurface temperatures are significantly correlated to the maximum poleward meridional velocities, representing the CUC core, during ENSO events. Following an El Niño event, a passing downwelling Kelvin wave deepens the CUC core and increases the subsurface temperature in N-CCS (Figure 3f). This is shown through the positive correlations of the depth of CUC in MJJ (when the seasonal difference in CUC depth between El Niño and La Niña is maximum; Figure S5) to the OND prior Niño 3.4 SST anomalies (Figure 5). The opposite happens during La Niña events, when the CUC core shoals along with an



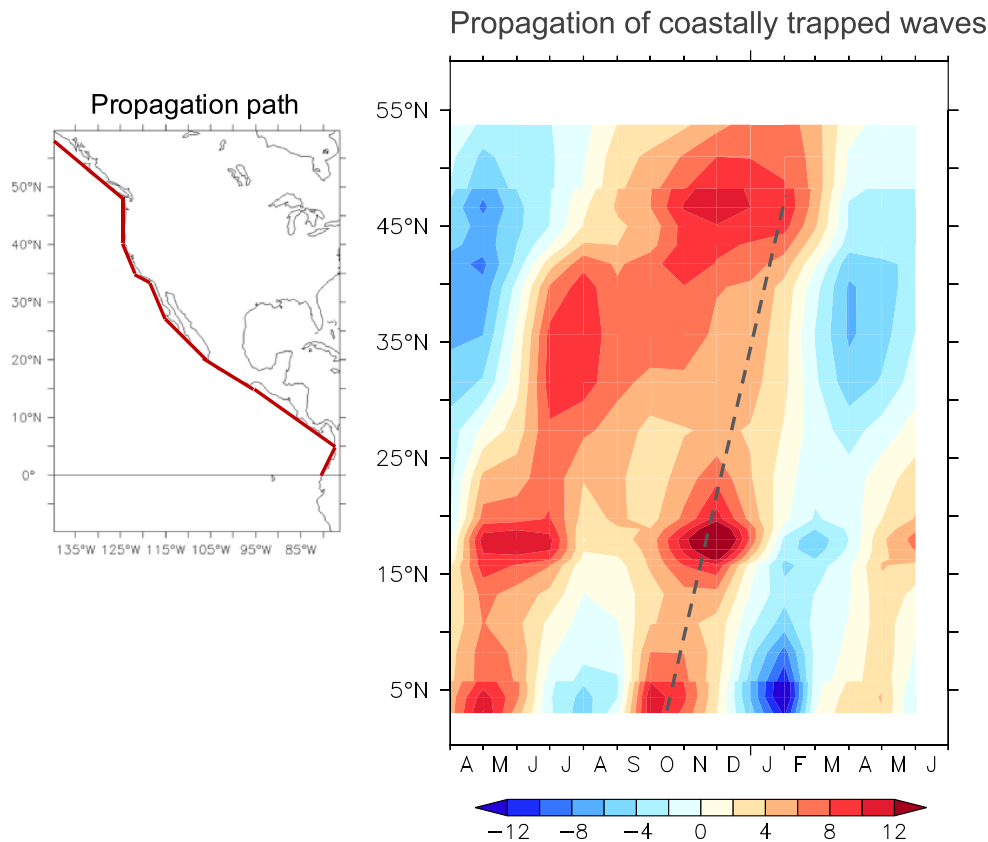


**Figure 4.** Hovmöller diagram of coastal Kelvin waves along the coast from equator to 60°N. Colors indicate composite of  $26.4\sigma$  monthly depth anomalies of 18 ENSO events (10 El Niño + 8 La Niña events) ranging from April of Year (0) to June of Year (1) along a curve line running along the coast (shown in left panel). A boxcar smoothing of 4 points (equivalent to 2° in y-direction) is applied in latitudinal direction to smooth out the rugged coastline in a coarse resolution model. The dashed line is indicative of the propagation. Propagation of equatorial Kelvin waves to around 45°N is clear with a lag of 4+ months.

upwelling Kelvin wave and cools the subsurface in the N-CCS. Thus, the depth of the CUC is an important input in the MLR, and due to its strong association to Niño 3.4 SST variation, it is also represented through the *Nino3* as a potential predictor in the linear regression model.

### 3.3.3. Regional Influence on Time Scales <3 Years

On advective time scales, spicy equatorial waters transported via CUC (0.01–0.03 m/s poleward mean current) from south of the N-CCS region could affect the subsurface temperature, at a 1- to 3-year lag, depending on how much of the equatorial properties are retained while dissipation processes act on the water properties moving northward. While the CFSR simulation of the poleward CUC is unrealistically weak, it may still be representative of the region of influence on temperatures in the CCS. Significant correlations of N-CCS TD to spice emerge at the south-west corner of the N-CCS region 3 years prior and amplify offshore across the U.S. West Coast from 32°N to 55°N within 2-year lag (Figures 6a and 6b). The significant correlations to spiciness anomalies south of N-CCS strengthen as time moves from a 2-year lag to no lag (Figures 6c and 6d), indicating that the region south of the N-CCS region is influential on N-CCS TD variations. The averaged  $26.4\sigma$  spice anomalies just south offshore of N-CCS are selected as potential predictors for MLR *SB2*, *SBI* (green boxes in Figures 6b and 6c).

### 3.3.4. Influence of the Central and Western Pacific

Oceanic processes that occur on longer time scales may also influence temperatures in the N-CCS region. A lag of 5–7 years is consistent with advection of water masses from around 160°E in the western Pacific to 126°W in the N-CCS domain, with the mean current decreasing from 0.07 (dateline) to 0.01 m/s close to the U.S. West Coast. That being said, this lag could also be generated by basin-wide phenomena that vary over time, that is, oscillate in place. In our analysis, negative spice anomalies in 1983 emerge from the Kuroshio region, suggesting propagation eastward, which would take almost 8 years to reach close to the

Influence of Niño 3.4 SST on CUC depth

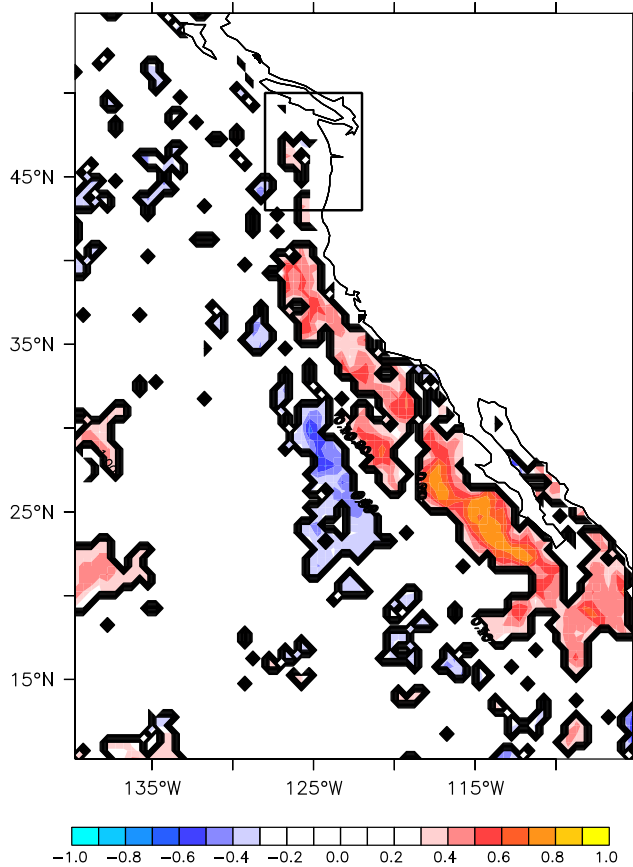


**Figure 5.** Niño 3.4 SST anomaly correlation to the anomaly of the depth of CUC core in CFSR. Shading indicates the magnitude of the correlation between OND Niño 3.4 SST anomaly to the following MJJ CUC depth along the U.S. West Coast. Regions with 90% significant correlations are enclosed by bold black contours. Positive correlations in the following summer indicate the influence of ENSO on the depth of CUC in the regions south of N-CCS.

mechanism by which it influences the subsurface in the N-CCS is not well known. The predictor is referred to as *PDO7*.

### 3.4. Linear Regression Model

#### 3.4.1. Selection of Variables

Regions identified with 90% significant correlations greater than 0.5 in both space and time (Figures 6 and 8) and described above are included as possible predictor variables for the stepwise MLR (Table 1).

The MLR model selection using annually smoothed time series of variables listed in Table 1 has an AIC score of  $-688.04$ . Collinearity tests reveal that *SCP5* has the highest VIF score (6.5), indicating that *SCP5* should be excluded for the next iteration of the MLR as it varies collinearly with other MLR variables. Proceeding with the predictors *WP6*, *SCP4*, *SBI*, *PDO4*, and *Nino3* in the next iteration, the stepwise MLR now indicates a better fit with a decrease in AICc score ( $-734.42$ ). Collinearity tests reveal that *SBI* (2.97), *WP6* (2.69), and *SCP4* (1.98) have comparable VIF scores, which indicates a linear dependence among the three variables. In the next iteration, proceeding with *WP6*, *SCP4*, *PDO4*, and *Nino3* as predictor variables, the stepwise MLR indicates a poor fit with an increase in AICc score ( $-513.75$ ). Thus, we proceed with *WP6*, *SCP4*, *SBI*, *PDO4*, and *Nino3* as our selected predictors for the MLR of annually smoothed N-CCS TD as chosen by the lowest AICc score.

U.S. West Coast in 1990 (Figure 7). Similarly, positive spice anomalies in 1991 and 2009 cross the North Pacific over time intervals of almost 8 and 6 years to reach the U.S. West Coast in 1999 and 2016, respectively (Figure 7). The influence of the spice anomalies from western Pacific on the N-CCS TD is also seen through the spatial patterns of its lag correlations to the N-CCS TD variations (Figure 8). The lag correlations of spice anomalies in the North Pacific to subsurface temperatures averaged in a domain spanning  $138^{\circ}\text{W}$  to  $132^{\circ}\text{W}$ ,  $45^{\circ}\text{N}$  to  $52^{\circ}\text{N}$ , offshore from N-CCS are stronger (not shown), indicating a stronger influence of western and central Pacific anomalies on subsurface temperatures northward of N-CCS. However, given N-CCS TD variability as the predictand, we select averaged  $26.4\sigma$  spiciness anomalies in regions of significant correlations in the western (*WP6*, *WP5*, Figures 8b and 8c) and central (*SCP5*, *SCP4*, Figures 8c and 8d) North Pacific to represent either an eastward advection oceanic teleconnection or the importance of a basin-wide oscillation at their respective time lags for inputs for the linear regression model (boxed regions in Figure 8).

#### 3.3.5. PDO Subdecadal Variability

Year round, PDO exhibits weak but significant correlations with seasonal N-CCS TD anomalies. The PDO tends to lead the N-CCS, with correlation coefficients exceeding 0.4 with the PDO beginning 4 months prior (Figure 9). Given that ENSO and the PDO exhibit their strongest influence on the North Pacific during the winter, it is very likely that some of the predictability from these two variables extends below the surface. A 4-month lag approximately coincides with influence from the winter ENSO and PDO to the TD in summer. On seasonal time scales, the N-CCS subsurface anomaly thus lags the PDO by 4 months ( $\text{corr} = 0.5$ ), and we refer to the 4-month lagged PDO as *PDO4* for the linear regression model.

On longer time scales, the PDO correlates significantly to the  $26.4\sigma$  temperature anomaly along the CCS with a 6- to 7-year lag, but with a change in sign (not shown). The spice in the N-CCS region as well as a region to the south is correlated to low-frequency PDO variability at 5- to 7-year lag (Figure 10). Hence, PDO at a lag of 7 years is also considered as a potential predictor in the linear regression model analysis, although the particular

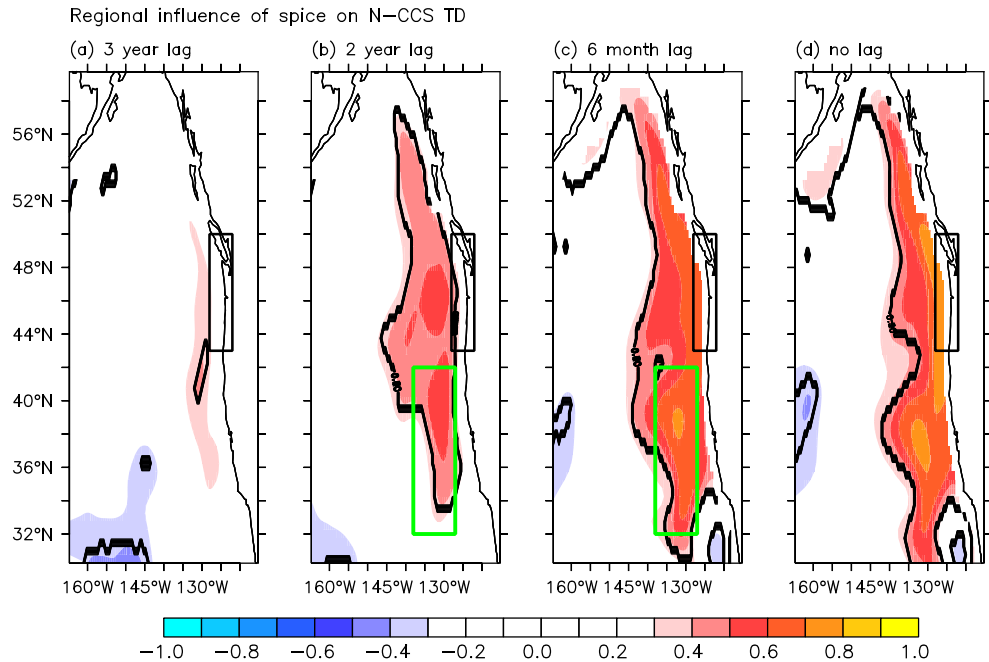


**Figure 6.** Regional influence within the CCS on time scales <3 years. Spatial correlations of monthly spice anomaly along  $26.4\sigma$  to monthly N-CCS TD anomaly at (a) 3 years, (b) 2 years, (c) 6 months, and (d) no lag. All months for the period 1979–2017 are considered in the analysis. Shading indicates the magnitude of the correlations overlaid with 90% significant contour in bold black. N-CCS domain is in black box, and regions of potential predictors, *SBI* (c) and *SB2* (b), are highlighted by the green boxes.

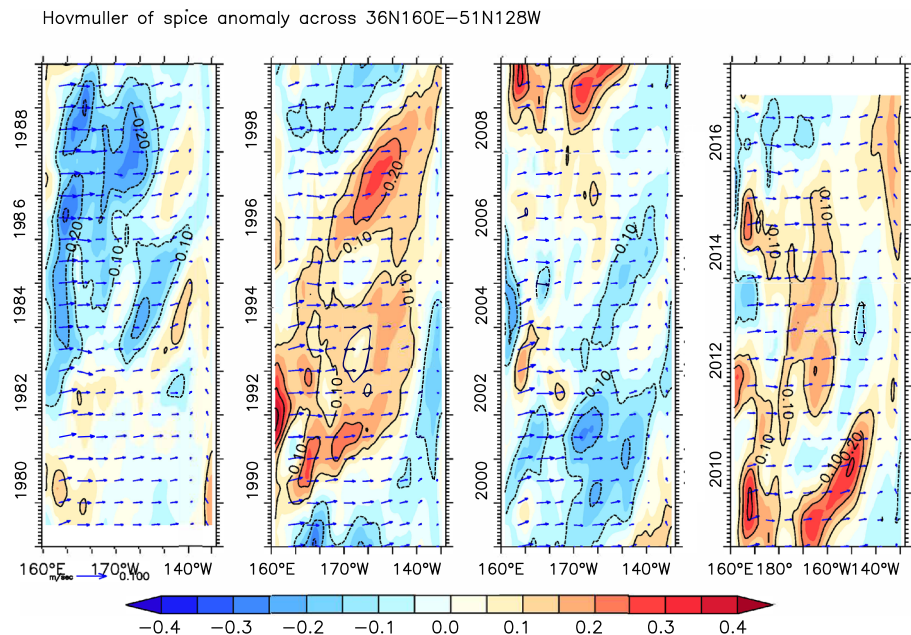


**Figure 7.** Hovmüller diagram indicating north-eastward advection across the Pacific. Shading indicates annually smoothed monthly spice anomaly along  $26.4\sigma$  across a north-eastward diagonal section ( $36^{\circ}\text{N}, 160^{\circ}\text{E}$  to  $51^{\circ}\text{N}, 128^{\circ}\text{W}$ ), cutting across the North Pacific (dash in Figure 8a), connecting the Kuroshio region to the U.S. West Coast. Individual decades spanning 1979–2017 are shown separately in each panel overlaid by the mean currents along  $26.4\sigma$ . Shading is incremented every half a contour. A smoothing of 12 months is applied.

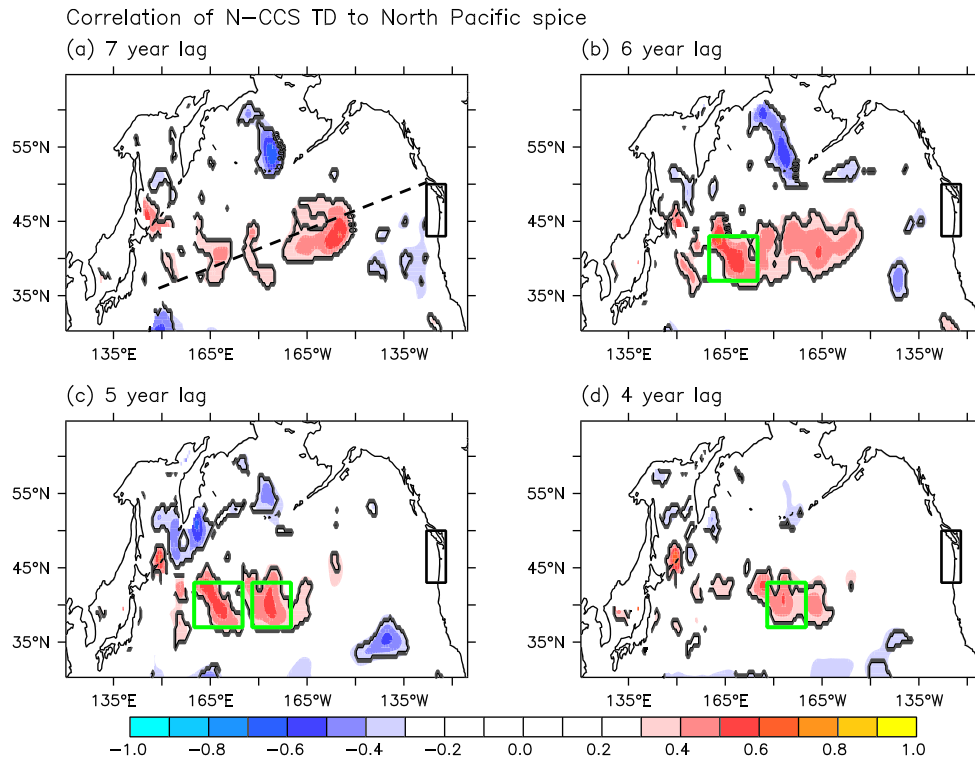


**Figure 8.** Influence of large-scale North Pacific spice anomalies along  $26.4\sigma$  to the N-CCS TD. Shading indicates the magnitude of spatial correlations between annual spice anomalies along  $26.4\sigma$  in the North Pacific and N-CCS TD at lag of (a) 7, (b) 6, (c) 5, and (d) 4 years, as indicated above each panel. Regions with 90% significant correlations are enclosed by bold black contours. The N-CCS domain is highlighted in black box. The black dash in (a) denotes the diagonal along which the Hovmöller of Figure 7 is done. The green boxes denote regions whose spatial averages are used as potential predictors for the linear regression model, namely, *WP6* in (b), *WP5* and *SCP5* in (c), and *SCP4* in (d).

### 3.4.2. MLR Explaining N-CCS TD

$$AnnualTD_{CFSR} = 0.53SB1 + 0.2PDO4 + 0.18Nino3 + 0.13WP6 + 0.06SCP4 \quad (1)$$

$$MonthlyTD_{CFSR} = 0.5SB1 + 0.14PDO4 + 0.25Nino3 + 0.09WP6 + 0.08SCP4 \quad (2)$$

The MLR model successfully explains a high percent of the annually smoothed N-CCS TD variability. The linear combination of these predictor variables (*WP6*, *SCP4*, *SBI*, *PDO4*, *Nino3*) explains 82.9% of the annually smoothed N-CCS TD variance, with a minimal root mean square error of 0.092 (Figure 11). The stepwise linear model reconstructs a 12-month smoothed TD model variation clearly giving relatively more importance to *SBI*, followed by *PDO4*, *Nino3*, *WP6*, and *SCP4*, as seen through their normalized coefficients 0.53, 0.2, 0.18, 0.13, and 0.06, respectively (Equation 1). The same predictors (*SBI*, *PDO4*, *Nino3*, *WP6*, *SCP4*) were chosen by the stepwise MLR when the monthly TD record was used as well. The monthly MLR explains 72.7% of the N-CCS TD variance (Figure 12), with an increase in the relative importance of the *Nino3* (0.25) predictor by 34.5% (normalized coefficients are 0.5, 0.09, 0.08, and 0.14 for *SBI*, *Kuro6*, *SCP4*, and *PDO4*) (Equation 2). Predictors representing oceanic teleconnections influential on longer than seasonal time scales (*WP6*, *SCP4*, *SBI*) explain 68.3% of the annually smoothed N-CCS TD variance. An MLR with only *WP6* and *SCP4* as variables explains 59.3% of the annually smoothed N-CCS TD variance, indicating a larger role of west-central Pacific spice anomalies through either eastward advection mechanism or a basin-wide oscillation at 6- and 4-year time lag on annually smoothed TD variance. The spiciness in the domain of *SBI* shows significant correlation to the low-frequency PDO variability (Figure 10) at a lag of 5–7 years and is the most important predictor at a lag of 6 months in both annual and monthly MLR. The importance of this predictor is validated in an independent data set, as shown in section 3.5. More than half of N-CCS TD variance is explained by oceanic teleconnections from North Pacific PDO, west-central Pacific spice, and spice from south of the domain.



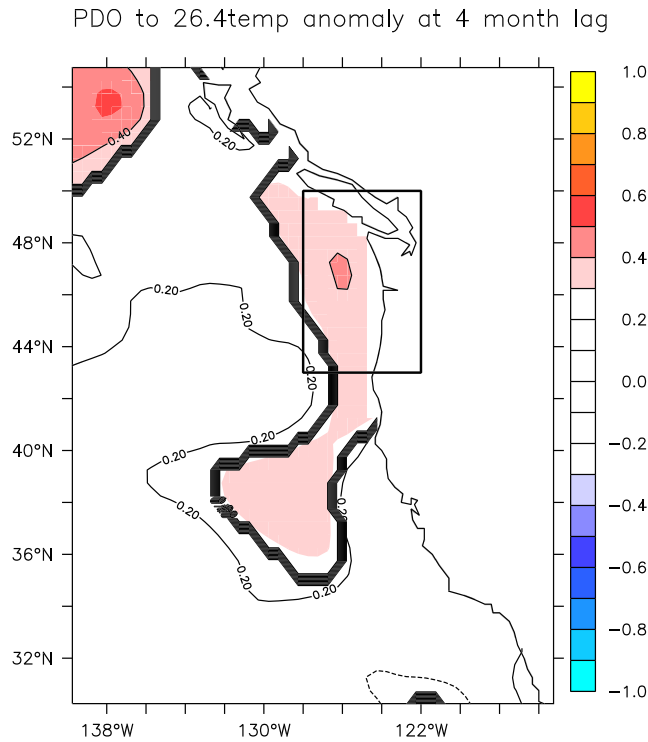


**Figure 9.** Seasonal PDO correlation to temperatures in CCS. Contours indicate the magnitude of the correlation between monthly  $26.4\sigma$  temperature anomalies and PDO at 4-month lag. Shading is incremented every half a contour (thin black) and contoured with 90% significance in bold black. N-CCS domain is identified by the black box.

### 3.5. Evaluation of the MLR Performance with SODA 3.4.2

The evaluation of the MLR with an external data set was performed in two ways. First is direct comparison of the performance of the MLR model with same coefficients as in Equation 1 from CFSR, but with the fields from SODA 3.4.2. The MLR explains only 50% of the annually smoothed N-CCS TD variance in SODA 3.4.2 (Figure S6). The difference in the model performance could stem from the differences between the evolution of subsurface temperatures and dynamics in CFSR and SODA 3.4.2, which could be generated from a combination of the differences in the ocean models upon which they are based, their respective resolutions, and assimilation methods. The  $26.4\sigma$  isopycnal in SODA 3.4.2 is deeper in the North Pacific, but is shallower in the N-CCS region when compared to CFSR (Figure S7). The monthly N-CCS TD variations are different among the reanalyses, as well, with SODA 3.4.2 producing a smaller range of variability (standard deviation 0.29) than CFSR (standard deviation 0.18).

$$AnnualTD_{SODA} = 0.89SB1 + 0.18PDO4 + 0.14Nino3 - 0.23WP6 + 0.21SCP4 \quad (3)$$

The performance of the selected predictors (*SB1*, *PDO4*, *Nino3*, *WP6*, *SCP4*) was also evaluated using SODA 3.4.2, but while the predictors remained the same as Equation 1 from CFSR, the coefficients were altered to fit the N-CCS TD in SODA 3.4.2. This way, the relative importance of the predictors is evaluated, but adjustments in fit were allowed to compensate for model differences described above that could influence the results. The MLR coefficients based on SODA 3.4.2 yield a primary result similar to that based on the CFSR, with *SB1* having the largest coefficients and hence serving as the most important predictor (Equation 3). The *Nino3* and *SCP4* predictors were of lesser and greater importance, respectively, in the model based on SODA 3.4.2 relative to its counterpart using CFSR. Note the opposite sign in *WP6*, suggesting the predictor to represent some local oscillation. In terms of overall performance, the MLR composed of predictors identified in CFSR and coefficients specific to SODA 3.4.2 (Equation 3) explains 71.5% of the annually smoothed N-CCS TD variance in SODA 3.4.2 (Figure 13).

The MLR composed of predictors identified in CFSR and coefficients specific to SODA 3.4.2 (Equation 3) explains 71.5% of the annually smoothed N-CCS TD variance in SODA 3.4.2 (Figure 13).

### 3.6. Evaluation of the MLR in Time

The CFSR data set was temporally divided into two periods: 1979–2010 to build the MLR and 2011–2017 to evaluate the newly trained MLR. The MLR using the predictors identified from the full temporal record spatial correlation analysis (*SB1*, *PDO4*, *Nino3*, *WP6*, *SCP4*) was retrained, thus redetermining the coefficients to fit the N-CCS TD in CFSR from 1979 to 2010. The new MLR was then compared to the 2011–2017 period to evaluate the MLR performance in time in both monthly and annually smoothed time series. The new MLR (Equations 4 and 5) coefficients support the primary result from the MLR derived over the entire time record: the *SB1* predictor has the largest coefficient and hence serves as the most important predictor (Equations 4 and 5). Although the relative importance of the *Nino3*, *WP6*, and *SCP4* remains almost unaltered (compared to Equations 1 and 2), the relative importance of *PDO4* decreased. The new coefficients derived over this shorter time interval (Equations 4 and 5) are then used to assess the performance of the MLR over the period 2011–2017 in reproducing the variability in the N-CCS TD.

$$AnnualTD_{1979-2010} = 0.52SB1 + 0.13PDO4 + 0.2Nino3 + 0.09WP6 + 0.07SCP4 \quad (4)$$

$$MonthlyTD_{1979-2010} = 0.47SB1 + 0.08PDO4 + 0.26Nino3 + 0.05WP6 + 0.09SCP4 \quad (5)$$

The MLR determined over the period 1979–2010 (Equations 4 and 5) explains 71.6% of the annually smoothed N-CCS TD variance (Figure 11) and 60% of the monthly variance in CFSR (Figure 12). Over the

Correlation of PDO to 26.4-spice anomaly beyond a year

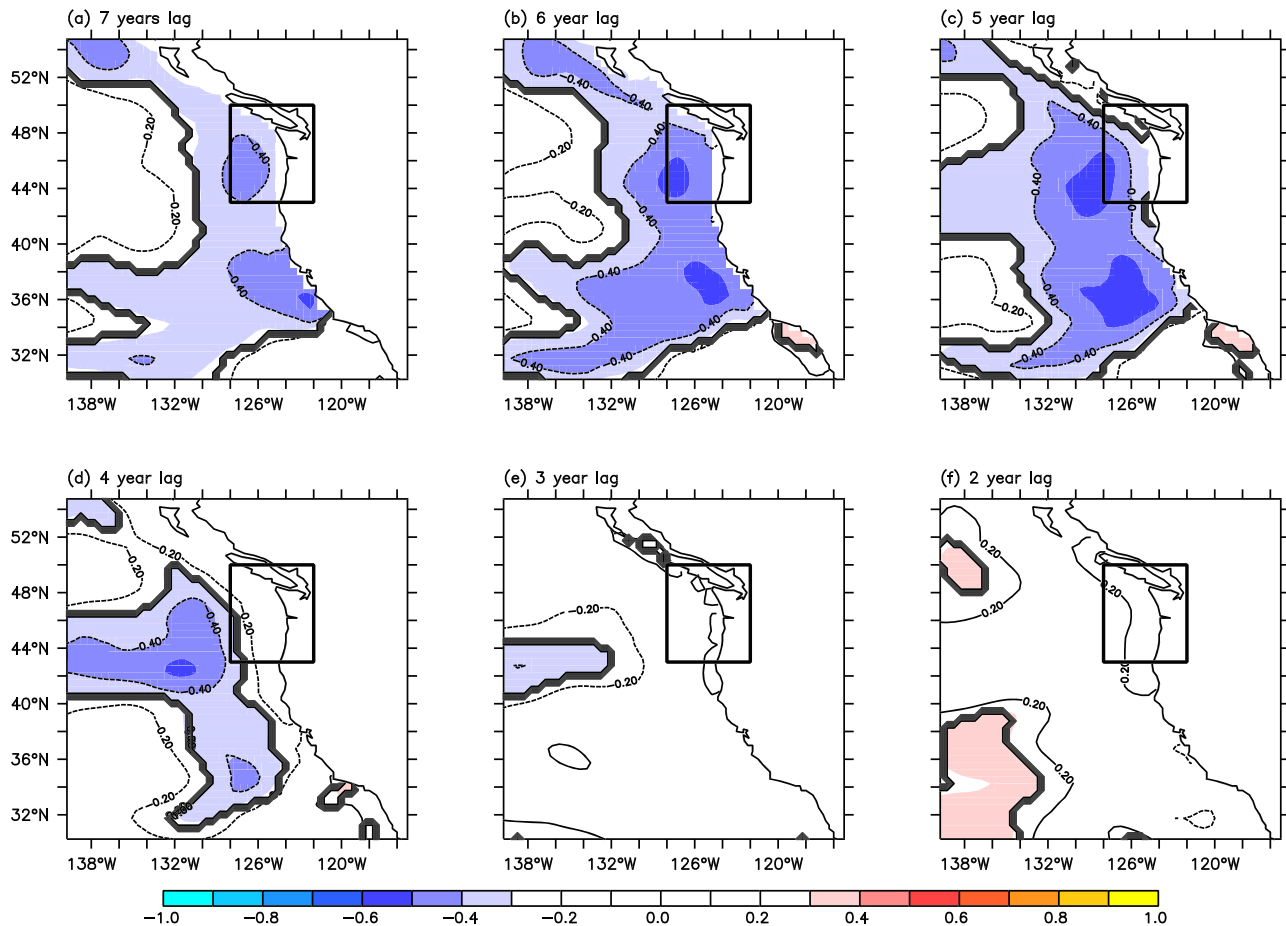


**Figure 10.** PDO correlation to spice anomaly in the CCS. Contouring indicates the magnitude of the correlations between monthly 26.4 $\sigma$  spice anomaly and the PDO at lags of (a)7, (b) 6, (c) 5, (d) 4, (e) 3, and (f) 2 years. Shading is incremented every half a contour (thin black) and enclosed with region of 90% significance in bold black contour. N-CCS domain is identified by a black box.

period 2011–2017, the MLR in Equation 4 explains 91.96% of the annually smoothed N-CCS TD variance (Figure 11) and 86.9% of the monthly N-CCS TD variance (Figure 12).

#### 4. Discussion

Spatial and temporal correlations of CFSR isopycnal depth and spice variability in the North and Tropical Pacific reveal the relative influence of known oceanic teleconnections to N-CCS TD over the period 1979–2017. Five predictors were identified by the spatial correlation analysis and then were chosen by the stepwise MLR based on AICc scores, including known influential oceanic teleconnections for the CCS: (i) the spiciness anomalies from west-central Pacific at a lag of 6 years and (ii) ENSO oceanic connection via CTWs at a lag of 4 months. Results indicate the strong influence of North Pacific variability on the TD variability in the N-CCS. This result is consistent with recent work (Capotondi et al., 2019) suggesting that the sensitivity of the U.S. West Coast SST could also come from the North Pacific and Tropical Pacific spatial patterns of SST and SSH, thus extending the source of predictability beyond solely ENSO events. The predictors identified here differ from predictors of SST variability over the entire Pacific identified in prior work, as well as the drivers of SST within CCS (Jacox et al., 2017), but the drivers of surface and subsurface variability are known to differ (Hickey et al., 2016).

The MLR explains 83% of the annually smoothed and 73% of the monthly N-CCS TD variability between 1979 to 2017, leaving about 17–27% of the variability unexplained here. This unexplained variability is

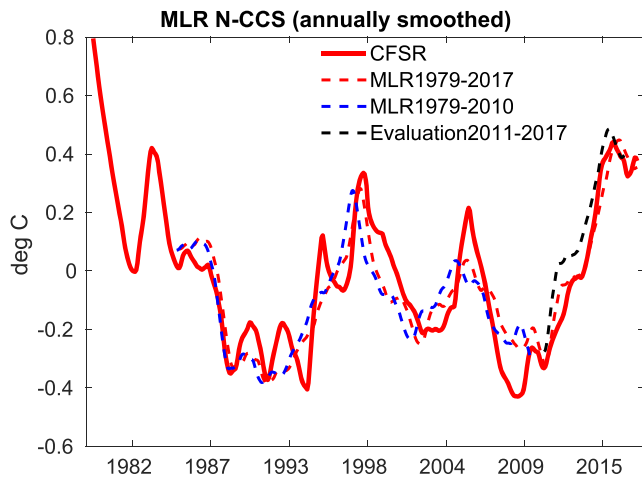


**Figure 11.** Annually smoothed N-CCS TD anomaly from CFSR (line) and the MLR reconstructing it (dash) using annually smoothed predictors (*WP6*, *SCP4*, *SBI*, *PDO4*, *Nino3*). Variance of 82.9% of the annually smoothed N-CCS TD is explained by the MLR (1979–2017) (Equation 1) with an RMS error = 0.092 (red dash). Refitting the MLR (Equation 4) with the same selected predictors from 1979 to 2010 (blue dash) explains 71.6% of the annually smoothed N-CCS TD variance, and evaluating this refitted MLR over the period 2011–2017 (black dash) explains 91.96% of the annually smoothed N-CCS TD variance in CFSR.

equatorial Pacific and consequent rectification of isopleths in the N-CCS. But that does not rule out the possible influence of locally generated CTW. For the neutral years, there is a high correlation ( $\sim 0.6$ ) between the variations in N-CCS  $26.4\sigma$  variations and the alongshore wind stress south of the domain (not shown). This suggests that the local generation of CTWs could occur during neutral years as a result of local along-shore wind variations. Remotely driven CTW also modulates the depth of CUC (Connolly et al., 2014; Stone et al., 2018), whose rectified effects persist through to the next summer after ENSO years. In our results, this

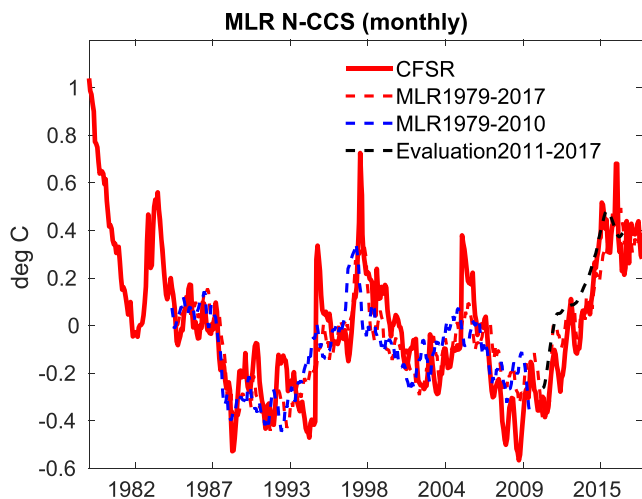


**Figure 12.** Monthly N-CCS TD anomaly from CFSR (line) and the MLR reconstructing it (dash) using monthly predictors (*WP6*, *SCP4*, *SBI*, *PDO4*, *Nino3*). Variance of 72.7% of the monthly N-CCS TD is explained by the MLR (1979–2017) (Equation 2) with an RMS error = 0.13 (red dash). Refitting the MLR (Equation 5) with the same selected predictors from 1979 to 2010 (blue dash) explains 60% of the monthly N-CCS TD variance, and evaluating this refitted MLR over the period 2011–2017 (black dash) explains 86.9% of the monthly N-CCS TD variance in CFSR.

likely due to local processes including air-sea interactions and nonlinear interactions between the terms, neither of which were considered here. Part of the difference in performance between the annual and monthly MLRs comes from the time scales of influence of the predictors and will be discussed more below. The MLR is evaluated with an independent data set, and the same ranking of predictors is identified.

Predictors with longer time lags of influence on the N-CCS TD, like *WP6* (6-year lag), are more important in the annual MLR than in the monthly MLR. The predictor variables *WP6* and *SCP4* in the MLR identify either that the spice anomalies originating in the west-central Pacific are advected via mean currents or represent a basin-wide phenomena that vary over time (Figures 7 and 8). This signal requires between 5 to 7 years to reach the U.S. West Coast, and as such, this decadal signal is a source of potential predictability to the N-CCS subsurface conditions. This is consistent with an eastward propagation of water mass anomalies along the sub-polar gyre which influences long-term oxygen variability (1950–2010) in the CCS (Pozo Buil & Di Lorenzo, 2017). Other mechanisms are more relevant to variability on seasonal time scales including several related to ENSO.

In the monthly MLR, the *Nino3* (4-month lag) predictor is much more important than in the annual MLR. This could be due to a combination of the atmospheric teleconnection and the CTW; however, the time scale is consistent with the transmission of remotely generated CTWs from the equatorial Pacific and consequent rectification of isopleths in the N-CCS. But that does not rule out the possible influence of locally generated CTW. For the neutral years, there is a high correlation ( $\sim 0.6$ ) between the variations in N-CCS  $26.4\sigma$  variations and the alongshore wind stress south of the domain (not shown). This suggests that the local generation of CTWs could occur during neutral years as a result of local along-shore wind variations. Remotely driven CTW also modulates the depth of CUC (Connolly et al., 2014; Stone et al., 2018), whose rectified effects persist through to the next summer after ENSO years. In our results, this mechanism was identified in the correlations of OND Niño 3.4 SST anomaly to the following MJJ depth of the CUC (lag of 4 months; Figure 5) south of N-CCS. Absence of such correlations following neutral years emphasizes the importance of ENSO to the remotely generated CTW signal.

In models of the N-CCS, generation of the CUC equally depends on CTW energy from the southern boundary, a remote mechanism (Connolly et al., 2014), and bathymetric details of the shelf and slope, a local process (Bograd et al., 2019; Durski et al., 2017; Hickey et al., 2016; Thomson & Krassovski, 2010). The nonlinear interactions between the large-scale mechanisms and the local processes have not been considered here, and instead, our focus is on the remote signals. The remote teleconnections explain between 73% to 83% of the TD variability. What is clear from the analysis is that CTW and/or their interactions with the CUC play an important role in driving subsurface temperature variability in the N-CCS on seasonal time scales.

The N-CCS TD is influenced by equatorial Pacific variability during ENSO much like SST, but with different prevailing transmission mechanisms and associated time scales. Although predictors for CCS SST variance include a 6-month lag ENSO index (Jacox et al., 2018), our analysis identifies a 4-month lag for N-CCS TD variance. The difference in time scales could be due to different pathways of influence, as well as the specific data used. The 6-month lag (Jacox et al., 2018) is consistent with the

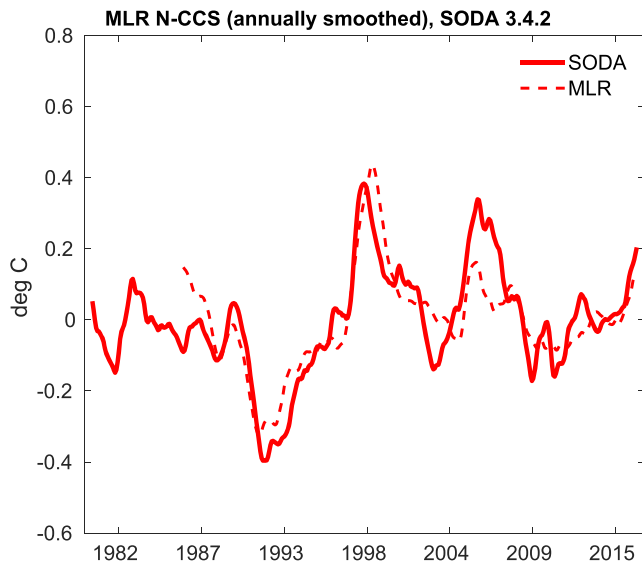


**Figure 13.** Annually smoothed N-CCS TD anomaly from SODA 3.4.2 (line) and the MLR reconstructing it (dash) using annually smoothed predictors identified in CFSR (*WP6*, *SCP4*, *SBI*, *PDO4*, *Nino3*) but sampled with SODA 3.4.2. In this comparison, the coefficients were fit to the annually smoothed N-CCS TD from SODA 3.4.2 (Equation 3). The N-CCS TD variability is different in CFSR than in SODA 3.4.2 (Figure S7). Variance of 71.5% of the N-CCS TD is explained by the MLR with an RMS error = 0.0879.

atmospheric pathway of ENSO influence (Alexander et al., 2002) and is an important driver for CCS SST (Jacox et al., 2017). The 4-month time scale identified here is closer to the time scale expected for the oceanic pathway of CTW transmission described above. In addition, damped persistence dominates SST variance (Jacox et al., 2018), but was not identified as a predictor (*persis*) in N-CCS TD MLR, although the comparison is not exact, as Jacox et al. (2018) used lag-1 autocorrelation for damped persistence. SST variance predictors tested in Jacox et al. (2018) did not include predictors with variability on near decadal time scales, suggesting that the damped persistence explicitly identified in their analysis could be a proxy for the long-term variability included in our analysis. Our analysis identifies the sensitivity of N-CCS TD to subsurface spatial patterns of the same regions at different time scales. Persistence could be an important predictor at shorter time lags within a dynamically downscaled forecast simulation, something we did not explore here.

The S-CCS spice anomaly is the most important predictor in the MLR for N-CCS TD on both the annual and monthly models with a maximal correlation 6 months prior (Figure 6b). The evaluation of the MLR with an independent data set also verified the importance of S-CCS spice anomaly in the linear model. The spatial correlations are consistent with more than one mechanism, and with the tools used here, we cannot identify the main driver of that anomaly. This is the first time this precursory ocean condition has been shown to be so important, recognizing that prior work in the region has suggested that conditions further south influence the variability of ocean conditions in the N-CCS region (Connolly et al.,

2014; Stone et al., 2018). Potential mechanisms responsible for this signal include locally generated CTW and its interactions with the CUC, advection of spice in the CUC locally within the CCS, and interactions with the gyre circulation. The influence of spice anomalies south of the N-CCS region can be seen spanning time lags from 6 months to 3 years prior (Figure 6). At 3-year lag, spatially, the maximal correlations exist in offshore waters west and south of the N-CCS that may in part serve as a source for the CUC (Figure 6a).

Although Figure 10 pointed to the correlation of low-frequency variability (PDO) on the spiciness in the region south of N-CCS at 5- to 7-year lag, it does not establish the causality of such spiciness variations. Hence, although the region south of N-CCS remotely seem to influence the N-CCS TD anomalies within a 3-year time lag window, identification of the mechanism responsible for this signal requires further inquiry with higher resolution tools.

### 5. Conclusion

In conclusion, North Pacific and Tropical Pacific variability explains 73–83% of the N-CCS TD (TD, defined as the N-CCS domain averaged temperature along  $26.4\sigma$ ) variance during 1979–2017, with the North Pacific dominating the variability. The MLR model selected several previously identified teleconnections: (i) ENSO at 4-month lag, (ii) PDO at 4-month lag, (iii) spice anomalies from west-central Pacific region at 6-year lag representing either the eastward advection or a basin-wide oscillating phenomena, and (iv) S-CCS spice anomalies at 6-month lag—a relatively lesser known precursory condition. The order of importance of the predictors was verified in an independent data set that was not used in the linear model selection. The predictors selected for the MLR model include ENSO teleconnections via oceanic pathways from the Tropical Pacific on shorter time scales. In this teleconnection, CTWs generated remotely from the equator during ENSO influence the N-CCS TD. In addition, these waves modulate the depth of the CUC and impact the seasonal upwelling water properties in N-CCS. North Pacific teleconnection includes influence of west-central Pacific spice anomalies on longer time scales and the effect of PDO-associated variations on seasonal time scales. Although the region south of N-CCS influences the N-CCS TD anomalies 3 years prior, complete understanding of the mechanism responsible for this signal requires further inquiry. We included mostly known oceanic teleconnections in our analysis to determine their relative importance on monthly and



annual N-CCS subsurface temperature variations, but further investigation into some is needed. Further work is required to determine the relative contribution of the CTW generated from alongshore wind perturbation locally in the CCS versus the remote generation from the equatorial Kelvin waves, as well as the role of the advective contribution of CUC in a higher-resolution model that resolves the CUC. Whether the predictability within the J-SCOPE reforecasts is also driven remotely by the above mechanisms through the boundaries requires future analysis and would serve as a vital step in building our understanding of these experimental forecast systems. In addition, improved monitoring of the region just south of the N-CCS domain in the central CCS with assets that can be integrated into reanalysis and forecast systems would be expected to yield better predictions in N-CCS TD.

### **Appendix A: CFSR Performance in North Pacific**

In the equatorial Pacific, CFSR is warmer than observed temperatures above the seasonal thermocline and has a flatter thermocline in the eastern equatorial Pacific (Saha et al., 2010). However, CFSR provides reasonable simulation of equatorial Kelvin waves and ENSO and PDO modes of climate variability (Xue et al., 2011). The averaged upper 300 m temperature along the U.S. West Coast in CFSR is within  $\pm 0.5^{\circ}\text{C}$ , different to observations (Saha et al., 2010). Discontinuities found in many physical fields are due to their assimilation cycle (Decker et al., 2012). Here we provide an analysis of its simulation of the CUC within the N-CCS, that was not reported in previous studies. The seasonal variability in CUC depth and slope is controlled by the seasonal alongshore wind, the alongshore pressure gradient, and shedding of Rossby waves from the coast. The CUC strengthens and deepens in summer to early fall, consistent with observations in the region (Durski et al., 2017; Pierce et al., 2000; Thomson & Krassovski, 2010), although the CFSR representation is notably weaker than observed (not shown). In MJJ, the CUC in the CFSR shows a mean deepening from 400 (46°N) to 612 m (49°N), which quickly shoals and flattens in the following JAS season, while staying more than 200 m below the depth of  $26.4\sigma$  (Figure S3). JAS marks the peak season of upwelling, bringing deeper slope waters into the bottom shelf. The northward alongshore pressure gradient is at its peak, the slope of CUC relaxes and shoals in lieu with reversing direction of the winds (southward to northward). With a southward alongshore pressure gradient building up, the CUC shoals rapidly with strengthening of northward wind, in particular to the north of 48°N, countering the pressure gradient force (Hickey & Pola, 1983), and surfacing in late fall/early winter (OND), and merging with the poleward Davidson current. Both the late fall/early winter (OND) and early summer (MAM) seasons show a steep northward slope in the CUC depth within N-CCS, countering the southward alongshore gradient, that cuts through the N-CCS  $26.4\sigma$  depth (Figure S3). Following ENSO events, CUC core in the southern boundary deepens in the following MAM season. The largest difference is seen in JAS, when the northward pressure gradient is at its peak, and the CUC core deepens by 200 m following an ENSO in the northern boundary. The Hovmöller for the along coast current in JAS (Figure S4) on density layers at locations close to the coast spanning from 25°N to 50°N shows that the poleward current peaks between 25 to  $26.4\sigma$  density layers. The CUC in high-density, spicy water is clearly seen from 25°N to 45°N, north of which it rapidly shoals to fresher mintier water that is advected from north. The latitudinal span of N-CCS falls within a zone of rapidly shoaling CUC with strong seasonal variability in its core depth (Figures S3 and S4). The interannual shoaling and deepening of the core of CUC (in symbols) with years following a La Niña and El Niño event, respectively, are apparent in Figure S4.

#### **Acknowledgments**

We thank Antonietta Capotondi and Art Miller for their constructive comments in improving the paper. We also thank an anonymous reviewer for his/her comments. We like to thank Emily Norton for her contribution in processing J-SCOPE model output, the NOAA MAPP Marine Prediction Task Force for providing insights to the study, and James Carton for providing helpful assistance in handling SODA dataset. This study was supported by NOAA's Climate Program Office's Modeling, Analysis, Predictions, and Projections Program, grant NA17OAR4310112. Computations were done on the University of Connecticut HPC Storrs Cluster supercomputer system.

#### **Data Availability Statement**

CFSR data sets for analysis were obtained from <https://www.ncdc.noaa.gov/data-access/model-data/model-datasets/climate-forecast-system-version2-cfsv2> and SODA data sets from [https://www2.atmos.umd.edu/~ocean/index\\_files/soda3\\_readme.htm](https://www2.atmos.umd.edu/~ocean/index_files/soda3_readme.htm).

#### **References**

- Alexander, M. A., Bladé, I., Newman, M., Lanzante, J. R., Lau, N.-C., & Scott, J. D. (2002). The Atmospheric Bridge: The Influence of ENSO Teleconnections on Air–Sea Interaction over the Global Oceans. *Journal of Climate*, 15(16), 2205–2231. [https://doi.org/10.1175/1520-0442\(2002\)015<2205:tabtio>2.0.co;2](https://doi.org/10.1175/1520-0442(2002)015<2205:tabtio>2.0.co;2)
- Alexander, M. A., & Deser, C. (1995). A mechanism for the recurrence of wintertime midlatitude SST anomalies. *Journal of Physical Oceanography*, 25(1), 122–137. [https://doi.org/10.1175/1520-0485\(1995\)025<0122:AMFTRO>2.0.CO;2](https://doi.org/10.1175/1520-0485(1995)025<0122:AMFTRO>2.0.CO;2)

- Alexander, M. A., Deser, C., & Timlin, M. S. (1999). The reemergence of SST anomalies in the North Pacific Ocean. *Journal of Climate*, *12*(8), 2419–2433.
- Alexander, M. A., & Scott, J. D. (2008). The role of Ekman ocean heat transport in the Northern Hemisphere response to ENSO. *Journal of Climate*, *21*(21), 5688–5707.
- Bograd, S. J., Buil, M. P., Di Lorenzo, E., Castro, C. G., Schroeder, I. D., Goericke, R., et al. (2015). Changes in source waters to the Southern California Bight. *Deep Sea Research Part II: Topical Studies in Oceanography*, *112*, 42–52.
- Bograd, S. J., Schroeder, I. D., & Jacox, M. G. (2019). A water mass history of the Southern California current system. *Geophysical Research Letters*, *46*, 6690–6698. <https://doi.org/10.1029/2019GL082685>
- Bretherton, C. S., Widmann, M., Dymnikov, V. P., Wallace, J. M., & Bladé, I. (1999). The effective number of spatial degrees of freedom of a time-varying field. *Journal of Climate*, *12*(7), 1990–2009.
- Burnham, K. P., & Anderson, D. R. (2002). Model selection and multimodel inference, (2nd), *A practical information-theoretic approach*. New York: Springer.
- Byju, P., Dommenges, D., & Alexander, M. (2018). Widespread reemergence of sea surface temperature anomalies in the global oceans, including tropical regions forced by reemerging winds. *Geophysical Research Letters*, *45*, 7683–7691. <https://doi.org/10.1029/2018GL079137>
- Capotondi, A., Sardeshmukh, P. D., Di Lorenzo, E., Subramanian, A. C., & Miller, A. J. (2019). Predictability of US West Coast ocean temperatures is not solely due to ENSO. *Scientific Reports*, *9*(1), 10,993.
- Carton, J. A., Chepurin, G. A., & Chen, L. (2018). SODA3: A new ocean climate reanalysis. *Journal of Climate*, *31*(17), 6967–6983.
- Chenillat, F., Rivière, P., Capet, X., Di Lorenzo, E., & Blanke, B. (2012). North Pacific Gyre Oscillation modulates seasonal timing and ecosystem functioning in the California Current upwelling system. *Geophysical Research Letters*, *39*, L01606. <https://doi.org/10.1029/2011GL049966>
- Chhak, K., & Di Lorenzo, E. (2007). Decadal variations in the California Current upwelling cells. *Geophysical Research Letters*, *34*, L14604. <https://doi.org/10.1029/2007GL030203>
- Chhak, K., Di Lorenzo, E., Schneider, N., & Cummins, P. F. (2009). Forcing of low-frequency ocean variability in the northeast Pacific. *Journal of Climate*, *22*(5), 1255–1276.
- Combes, V., Chenillat, F., Di Lorenzo, E., Rivière, P., Ohman, M., & Bograd, S. (2013). Cross-shore transport variability in the California Current: Ekman upwelling vs. eddy dynamics. *Progress in Oceanography*, *109*, 78–89.
- Commission, I. O., Scientific Committee on Oceanic Research, & International Association for the Physical Sciences of the Oceans (2015). The international thermodynamic equation of seawater—2010: Calculation and use of thermodynamic properties.[includes corrections up to 31st October 2015].
- Connolly, T. P., Hickey, B. M., Shulman, I., & Thomson, R. E. (2014). Coastal trapped waves, alongshore pressure gradients, and the California Undercurrent. *Journal of Physical Oceanography*, *44*(1), 319–342.
- Crawford, W. J., Moore, A. M., Jacox, M. G., Fiechter, J., Neveu, E., & Edwards, C. A. (2018). A resonant response of the California Current circulation to forcing by low frequency climate variability. *Deep Sea Research Part II: Topical Studies in Oceanography*, *151*, 16–36.
- Decker, M., Brunke, M. A., Wang, Z., Sakaguchi, K., Zeng, X., & Bosilovich, M. G. (2012). Evaluation of the reanalysis products from GSFC, NCEP, and ECMWF using flux tower observations. *Journal of Climate*, *25*(6), 1916–1944.
- Deser, C., Alexander, M. A., & Timlin, M. S. (2003). Understanding the persistence of sea surface temperature anomalies in midlatitudes. *Journal of Climate*, *16*(1), 57–72.
- Di Lorenzo, E., Schneider, N., Cobb, K. M., Franks, P., Chhak, K., Miller, A. J., et al. (2008). North Pacific Gyre Oscillation links ocean climate and ecosystem change. *Geophysical Research Letters*, *35*, L08607. <https://doi.org/10.1029/2007GL032838>
- Durski, S. M., Barth, J. A., McWilliams, J. C., Frenzel, H., & Deutsch, C. (2017). The influence of variable slope-water characteristics on dissolved oxygen levels in the northern California Current System. *Journal of Geophysical Research: Oceans*, *122*, 7674–7697. <https://doi.org/10.1002/2017JC013089>
- Enfield, D. B., Cornejo-Rodriguez, M. D. P., Smith, R. L., & Newberger, P. A. (1987). The equatorial source of propagating variability along the Peru coast during the 1982–1983 El Niño. *Journal of Geophysical Research*, *92*(C13), 14,335–14,346.
- Engda, Z., Monahan, A., Ianson, D., & Thomson, R. E. (2016). Remote forcing of subsurface currents and temperatures near the northern limit of the California Current System. *Journal of Geophysical Research: Oceans*, *121*, 7244–7262. <https://doi.org/10.1002/2016JC011880>
- Flores-Morales, A. L., Parés-Sierra, A., & Gómez-Valdivia, F. (2012). Semiannual Kelvin waves in the northeastern tropical Pacific. *Journal of Coastal Research*, *28*(5), 1068–1072.
- Freeland, H. J., Gatién, G., Huyer, A., & Smith, R. L. (2003). Cold halocline in the northern California Current: An invasion of subarctic water. *Geophysical Research Letters*, *30*(3), 1141. <https://doi.org/10.1029/2002GL016663>
- Frischknecht, M., Münnich, M., & Gruber, N. (2015). Remote versus local influence of ENSO on the California Current System. *Journal of Geophysical Research: Oceans*, *120*, 1353–1374. <https://doi.org/10.1002/2014JC010531>
- Garfield, N., Maltrud, M. E., Collins, C. A., Rago, T. A., & Paquette, R. G. (2001). Lagrangian flow in the California Undercurrent, an observation and model comparison. *Journal of Marine Systems*, *29*(1–4), 201–220.
- Giddings, S., MacCreedy, P., Hickey, B., Banas, N., Davis, K., Siedlecki, S., et al. (2014). Hindcasts of potential harmful algal bloom transport pathways on the Pacific Northwest coast. *Journal of Geophysical Research: Oceans*, *119*, 2439–2461. <https://doi.org/10.1002/2013JC009622>
- He, X., & Guan, H. (2013). Multiresolution analysis of precipitation teleconnections with large-scale climate signals: A case study in South Australia. *Water Resources Research*, *49*, 6995–7008. <https://doi.org/10.1002/wrcr.20560>
- Hermann, A. J., Curchitser, E. N., Haidvogel, D. B., & Dobbins, E. L. (2009). A comparison of remote vs. local influence of El Niño on the coastal circulation of the northeast Pacific. *Deep Sea Research Part II: Topical Studies in Oceanography*, *56*(24), 2427–2443.
- Hervieux, G., Alexander, M., Stock, C., Jacox, M., Pegion, K., Becker, E., et al. (2017). More reliable coastal SST forecasts from the North American multimodel ensemble. *Climate Dynamics*, *53*, 7153–7168.
- Hickey, B., Dobbins, E., & Allen, S. E. (2003). Local and remote forcing of currents and temperature in the central Southern California Bight. *Journal of Geophysical Research*, *108*(C3), 3081. <https://doi.org/10.1029/2000JC000313>
- Hickey, B., Geier, S., Kachel, N., Ramp, S., Kosro, P., & Connolly, T. (2016). Alongcoast structure and interannual variability of seasonal midshelf water properties and velocity in the Northern California Current System. *Journal of Geophysical Research: Oceans*, *121*, 7408–7430. <https://doi.org/10.1002/2015JC011424>
- Hickey, B., MacFadyen, A., Cochlan, W., Kudela, R., Bruland, K., & Trick, C. (2006). Evolution of chemical, biological, and physical water properties in the northern California Current in 2005: Remote or local wind forcing? *Geophysical Research Letters*, *33*, L22S02. <https://doi.org/10.1029/2006GL026782>

- Hickey, B. M., & Pola, N. E. (1983). The seasonal alongshore pressure gradient on the West Coast of the United States. *Journal of Geophysical Research*, 88(C12), 7623–7633.
- Huyer, A. (2003). Preface to special section on enhanced subarctic influence in the California Current, 2002. *Geophysical Research Letters*, 30(15), 8019. <https://doi.org/10.1029/2003GL017724>
- Huyer, A., & Smith, R. L. (1985). The signature of El Niño off Oregon, 1982–1983. *Journal of Geophysical Research*, 90(C4), 7133–7142.
- Jacox, M. G., Alexander, M. A., Mantua, N. J., Scott, J. D., Hervieux, G., Webb, R. S., & Werner, F. E. (2018). Forcing of multiyear extreme ocean temperatures that impacted California Current living marine resources in 2016. *Bulletin of the American Meteorological Society*, 99(1), S27–S33.
- Jacox, M. G., Alexander, M. A., Siedlecki, S., Chen, K., Kwon, Y. O., Brodie, S., et al. (2020). Seasonal-to-interannual prediction of US coastal marine ecosystems: Forecast methods, mechanisms of predictability, and priority developments. *Progress in Oceanography*, 183, 102307.
- Jacox, M. G., Alexander, M. A., Stock, C. A., & Hervieux, G. (2017). On the skill of seasonal sea surface temperature forecasts in the California Current System and its connection to ENSO variability. *Climate Dynamics*, 53, 7519–7533.
- Jacox, M. G., Bograd, S. J., Hazen, E. L., & Fiechter, J. (2015). Sensitivity of the California Current nutrient supply to wind, heat, and remote ocean forcing. *Geophysical Research Letters*, 42, 5950–5957. <https://doi.org/10.1002/2015GL065147>
- Jacox, M. G., Fiechter, J., Moore, A. M., & Edwards, C. A. (2015). ENSO and the California Current coastal upwelling response. *Journal of Geophysical Research: Oceans*, 120, 1691–1702. <https://doi.org/10.1002/2014JC010650>
- Juranek, L., Feely, R., Peterson, W., Alin, S., Hales, B., Lee, K., et al. (2009). A novel method for determination of aragonite saturation state on the continental shelf of central Oregon using multi-parameter relationships with hydrographic data. *Geophysical Research Letters*, 36, L24601. <https://doi.org/10.1029/2009GL040778>
- Kaplan, I. C., Williams, G. D., Bond, N. A., Hermann, A. J., & Siedlecki, S. A. (2016). Cloudy with a chance of sardines: Forecasting sardine distributions using regional climate models. *Fisheries Oceanography*, 25(1), 15–27.
- Kirtman, B. P., Min, D., Infanti, J. M., Kinter III, J. L., Paolino, D. A., Zhang, Q., et al. (2014). The North American multimodel ensemble: Phase-1 seasonal-to-interannual prediction; Phase-2 toward developing intraseasonal prediction. *Bulletin of the American Meteorological Society*, 95(4), 585–601.
- Kosro, P. M. (2003). Enhanced southward flow over the Oregon shelf in 2002: A conduit for subarctic water. *Geophysical Research Letters*, 30(15), 8023. <https://doi.org/10.1029/2003GL017436>
- Kouketsu, S., Osafune, S., Kumamoto, Y., & Uchida, H. (2017). Eastward salinity anomaly propagation in the intermediate layer of the North Pacific. *Journal of Geophysical Research: Oceans*, 122, 1590–1607. <https://doi.org/10.1002/2016JC012118>
- Lyman, J. M., & Johnson, G. C. (2008). Equatorial Kelvin wave influences may reach the Bering Sea during 2002 to 2005. *Geophysical Research Letters*, 35, L14607. <https://doi.org/10.1029/2008GL034761>
- Lynn, R. J., Schwing, F. B., & Hayward, T. L. (1995). The effect of the 1991–1993 ENSO on the California Current System. California Cooperative Oceanic Fisheries Investigations Report.
- MacFadyen, A., Hickey, B. M., & Cochla, W. P. (2008). Influences of the Juan de Fuca eddy on circulation, nutrients, and phytoplankton production in the northern California Current System. *Journal of Geophysical Research*, 113, C08008. <https://doi.org/10.1029/2007JC004412>
- McCabe, R. M., Hickey, B. M., Dever, E. P., & MacCready, P. (2015). Seasonal cross-shelf flow structure, upwelling relaxation, and the alongshelf pressure gradient in the Northern California Current System. *Journal of Physical Oceanography*, 45(1), 209–227.
- McClatchie, S., Goericke, R., Schwing, F. B., Bograd, S. J., Peterson, W. T., Emmett, R., et al. (2009). The state of the California Current, spring 2008–2009: Cold conditions drive regional differences in coastal production. *Cooperative Oceanic Fisheries Investigations Reports*, 50, 43–68.
- McDougall, T. J., & Barker, P. M. (2011). *Getting started with TEOS-10 and the Gibbs Seawater (GSW) oceanographic toolbox*, SCOR/IAPSO WG, vol. 127, pp. 1–28.
- McDougall, T. J., & Krzysik, O. A. (2015). Spiciness. *Journal of Marine Research*, 73(5), 141–152.
- Meinvielle, M., & Johnson, G. C. (2013). Decadal water-property trends in the California Undercurrent, with implications for ocean acidification. *Journal of Geophysical Research: Oceans*, 118, 6687–6703. <https://doi.org/10.1002/2013JC009299>
- Melsom, A., Metzger, E. J., & Hurlburt, H. E. (2003). Impact of remote oceanic forcing on Gulf of Alaska sea levels and mesoscale circulation. *Journal of Geophysical Research*, 108(C11), 3346. <https://doi.org/10.1029/2002JC001742>
- Meyers, S. D., Melsom, A., Mitchum, G. T., & O'Brien, J. J. (1998). Detection of the fast Kelvin wave teleconnection due to El Niño–Southern Oscillation. *Journal of Geophysical Research*, 103(C12), 27,655–27,663.
- Newman, M., Alexander, M. A., Ault, T. R., Cobb, K. M., Deser, C., Di Lorenzo, E., et al. (2016). The Pacific Decadal Oscillation, revisited. *Journal of Climate*, 29(12), 4399–4427.
- Norton, E. L., Siedlecki, S., Kaplan, I. C., Hermann, A. J., Fisher, J. L., Morgan, C. A., et al. (2020). The importance of environmental exposure history in forecasting Dungeness crab megalopae occurrence using J-SCOPE, a high-resolution model for the US Pacific Northwest. *Frontiers in Marine Science*, 7, 102.
- Pelland, N. A., Eriksen, C. C., & Lee, C. M. (2013). Subthermocline eddies over the Washington continental slope as observed by Seagliders, 2003–09. *Journal of Physical Oceanography*, 43(10), 2025–2053.
- Pierce, S., Smith, R., Kosro, P., Barth, J., & Wilson, C. (2000). Continuity of the poleward undercurrent along the eastern boundary of the mid-latitude north Pacific. *Deep Sea Research Part II: Topical Studies in Oceanography*, 47(5-6), 811–829.
- Pozo Buil, M., & Di Lorenzo, E. (2017). Decadal dynamics and predictability of oxygen and subsurface tracers in the California Current System. *Geophysical Research Letters*, 44, 4204–4213. <https://doi.org/10.1002/2017GL072931>
- Ray, S., Swingedouw, D., Mignot, J., & Guilyardi, E. (2015). Effect of surface restoring on subsurface variability in a climate model during 1949–2005. *Climate Dynamics*, 44(9-10), 2333–2349.
- Rykaczewski, R. R., & Dunne, J. P. (2010). Enhanced nutrient supply to the California Current Ecosystem with global warming and increased stratification in an earth system model. *Geophysical Research Letters*, 37, L21606. <https://doi.org/10.1029/2010GL045019>
- Saha, S., Moorthi, S., Pan, H. L., Wu, X., Wang, J., Nadiga, S., et al. (2010). The NCEP climate forecast system reanalysis. *Bulletin of the American Meteorological Society*, 91(8), 1015–1058.
- Sasaki, Y. N., Schneider, N., Maximenko, N., & Lebedev, K. (2010). Observational evidence for propagation of decadal spiciness anomalies in the North Pacific. *Geophysical Research Letters*, 37, L07708. <https://doi.org/10.1029/2010GL042716>
- Schwing, F. B., Murphree, T., Dewitt, L., & Green, P. M. (2002). The evolution of oceanic and atmospheric anomalies in the northeast Pacific during the El Niño and La Niña events of 1995–2001. *Progress in Oceanography*, 54(1-4), 459–491.

- Siedlecki, S. A., Kaplan, I. C., Hermann, A. J., Nguyen, T. T., Bond, N. A., Newton, J. A., et al. (2016). Experiments with seasonal forecasts of ocean conditions for the northern region of the California Current upwelling system. *Scientific Reports*, *6*, 27,203.
- Stock, C. A., Pegion, K., Vecchi, G. A., Alexander, M. A., Tommasi, D., Bond, N. A., et al. (2015). Seasonal sea surface temperature anomaly prediction for coastal ecosystems. *Progress in Oceanography*, *137*, 219–236.
- Stone, H. B., Banas, N. S., & MacCready, P. (2018). The effect of alongcoast advection on Pacific Northwest shelf and slope water properties in relation to upwelling variability. *Journal of Geophysical Research: Oceans*, *123*, 265–286. <https://doi.org/10.1002/2017JC013174>
- Taguchi, B., & Schneider, N. (2014). Origin of decadal-scale, eastward-propagating heat content anomalies in the North Pacific. *Journal of Climate*, *27*(20), 7568–7586.
- Thomson, R. E., & Krassovski, M. V. (2010). Poleward reach of the California Undercurrent extension. *Journal of Geophysical Research*, *115*, C09027. <https://doi.org/10.1029/2010JC006280>
- Timmermans, M. L., & Jayne, S. R. (2016). The arctic ocean spices up. *Journal of Physical Oceanography*, *46*(4), 1277–1284.
- Tommasi, D., Stock, C. A., Hobday, A. J., Methot, R., Kaplan, I. C., Eveson, J. P., et al. (2017). Managing living marine resources in a dynamic environment: The role of seasonal to decadal climate forecasts. *Progress in Oceanography*, *152*, 15–49.
- Wilks, D. S. (1995). *Statistical methods in the atmospheric sciences, 1995* (pp. 465). San Diego, CA: Library of Cataloging-in-publication, Academic Press.
- Wills, R. C., Schneider, T., Wallace, J. M., Battisti, D. S., & Hartmann, D. L. (2018). Disentangling global warming, multidecadal variability, and El Niño in Pacific temperatures. *Geophysical Research Letters*, *45*, 2487–2496. <https://doi.org/10.1002/2017GL076327>
- Xue, Y., Huang, B., Hu, Z. Z., Kumar, A., Wen, C., Behringer, D., & Nadiga, S. (2011). An assessment of oceanic variability in the NCEP climate forecast system reanalysis. *Climate Dynamics*, *37*(11-12), 2511–2539.
- Yamashita, T., Yamashita, K., & Kamimura, R. (2007). A stepwise AIC method for variable selection in linear regression. *Communications in Statistics-Theory and Methods*, *36*(13), 2395–2403.